


## Self-consistent ladder dynamical vertex approximation

Josef Kaufmann<sup>1</sup>, Christian Eckhardt<sup>2,1</sup>, Matthias Pickem<sup>1</sup>, Motoharu Kitatani<sup>3</sup>, Anna Kauch<sup>1,\*</sup> and Karsten Held<sup>1</sup><sup>1</sup>Institute of Solid State Physics, TU Wien, 1040 Vienna, Austria<sup>2</sup>Institute for Theoretical Solid State Physics, RWTH Aachen University, 52074 Aachen, Germany<sup>3</sup>RIKEN Center for Emergent Matter Sciences (CEMS), Wako, Saitama 351-0198, Japan (Received 8 October 2020; revised 21 December 2020; accepted 22 December 2020; published 15 January 2021)

We present and implement a self-consistent D $\Gamma$ A approach for multiorbital models and *ab initio* materials calculations. It is applied to the one-band Hubbard model at various interaction strengths with and without doping, to the two-band Hubbard model with two largely different bandwidths, and to SrVO<sub>3</sub>. The self-energy feedback reduces critical temperatures compared to dynamical mean-field theory, even to zero temperature in two dimensions. Compared to a one-shot, non-self-consistent calculation the nonlocal correlations are significantly reduced when they are strong. In case nonlocal correlations are weak to moderate as for SrVO<sub>3</sub>, one-shot calculations are sufficient.

DOI: [10.1103/PhysRevB.103.035120](https://doi.org/10.1103/PhysRevB.103.035120)

## I. INTRODUCTION

Strongly correlated materials are becoming more and more relevant for technological applications. They are also utterly fascinating, not least because their theoretical study is intrinsically difficult. The actual calculation of correlated materials and their properties usually requires a combination of *ab initio* methods and simplified model approaches. A very successful *ab initio* method for studying strongly correlated materials is the combination of density functional theory [1,2] with the dynamical mean-field theory [3–7] (DFT + DMFT) [6–12], which is capable of describing local electronic correlations very accurately. In systems where nonlocal correlations play an important role, e.g., in two-dimensional or layered systems, DMFT cannot predict the correct low temperature behavior. Cluster and diagrammatic extensions of DMFT [13,14] have been developed to cure this problem.

One such method is the *ab initio* D $\Gamma$ A [15–17] which extends the concept of the dynamical vertex approximation (D $\Gamma$ A) [18,19] to realistic materials calculations. It inherits from DMFT the nonperturbative treatment of strong local correlations, but on top of this also includes nonlocal correlations. To this end, a two-particle ladder is built with the local DMFT irreducible vertex and the nonlocal Green's function as building blocks. These ladder diagrams then yield a nonlocal contribution to the self-energy.

Hitherto such *ab initio* D $\Gamma$ A calculations have been restricted to so-called “one-shot” calculations without an update of the DMFT vertex and nonlocal Green's function. Obviously, such a one-shot calculation is only expected to be reasonable as long as the nonlocal corrections to DMFT remain small. It also does not suppress the DMFT critical temperatures nor modifies the DMFT critical exponents. In the case of D $\Gamma$ A calculations for one-band models, so far

a Moriyaesque  $\lambda$  correction [19,20] was devised as a cure. It imposes a sum rule on the spin (or alternatively spin and charge) susceptibility, reduces the critical temperature, and yields reasonable critical exponents [21–23]. Superconductivity in cuprates [24] and nickelates [25] is described surprisingly accurately, even correctly predicted in the latter case. The extension to the multiorbital case, however, makes this Moriyaesque  $\lambda$  correction difficult. One would need to introduce and determine various  $\lambda$  parameters for all orbital combinations and spin channels. This would result in a multidimensional optimization problem that is likely to have several local optima of comparable quality; details of how the  $\lambda$  correction is modeled (which is nonunique) might be decisive.

Another route has been taken in the closely related dual fermion approach [26] with ladder diagrams [27]. Here, the Green's function is updated with the calculated nonlocal self-energy in a so-called “inner self-consistency.” Hitherto applied to one-band model Hamiltonians such as the Hubbard [28] and Falicov-Kimball model [29] yields very reasonable critical temperatures and exponents. Also a self-consistent update of the dual fermion vertex has been discussed [30–32].

In the case of D $\Gamma$ A such an update of the Green's function has also been made, however only for the much more involved parquet D $\Gamma$ A [33–38]. Here, besides the self-consistent update of the Green's function and self-energy, all three scattering (ladder) channels are mutually fed back into all other channels through the parquet equation [39–42]. The drawback is the extreme numerical effort needed to solve the parquet equations, which limits the method to one-band models so far [33,34,36,43].

In this paper we present a self-consistent ladder D $\Gamma$ A (sc-D $\Gamma$ A) for multiorbital models. We update the Green's function lines, as is also done in parquet and dual fermion approaches but neither in the original *ab initio* D $\Gamma$ A method nor in previous ladder D $\Gamma$ A calculations. This allows for a self-energy feedback into the ladder diagrams contained in

\*kauch@ifp.tuwien.ac.at

the Bethe-Salpeter equation and leads to substantial damping of the fluctuations in the respective scattering channel. Since this approach only requires a repeated evaluation of the *ab initio* D $\Gamma$ A equations, its application to multiorbital models is straightforward. Our results demonstrate that sc-D $\Gamma$ A works well for single- and multiorbital systems and also when doping away from integer filling.

The paper is organized as follows: In Sec. II we introduce the Hubbard model (HM), our notation, and the DMFT. Furthermore we give an overview over the different variants of D $\Gamma$ A that were hitherto used. In Sec. III we introduce our new way of doing D $\Gamma$ A self-consistently. Then, in Sec. IV, we present results for the single-orbital Hubbard model on the square lattice with nearest-neighbor hopping. This model has already been extensively studied and our results can be compared to the literature. Finally, in Sec. V, we present results for a two-orbital model system with Kanamori interaction and for SrVO<sub>3</sub> at room temperature.

## II. MODEL AND FORMALISM

### A. Multiorbital Hubbard model

The Hamiltonian of the multiorbital Hubbard model reads

$$H_{\text{HM}} = \sum_{\mathbf{k}} \sum_{lm\sigma} h_{lm}(\mathbf{k}) \hat{c}_{\mathbf{k}l\sigma}^\dagger \hat{c}_{\mathbf{k}m\sigma} + \sum_i \sum_{l'l'mm'} U_{lm'l'm'} \hat{c}_{il'm'}^\dagger \hat{c}_{il\sigma'}^\dagger \hat{c}_{im\sigma'} \hat{c}_{il'\sigma'}. \quad (1)$$

Here, the first term is the underlying tight-binding model, which can be obtained *ab initio* by Wannierization of a band structure from density functional theory. The operator  $\hat{c}_{\mathbf{k}m\sigma}^\dagger$  ( $\hat{c}_{\mathbf{k}m\sigma}$ ) creates (removes) an electron with spin  $\sigma$  in the Wannier orbital  $m$  at momentum  $\mathbf{k}$  (the Fourier transformed operators are labeled with unit cell index  $i$  instead of  $\mathbf{k}$ ). The second term of Eq. (1) contains the interaction of the electrons. While the underlying *ab initio* D $\Gamma$ A can in principle include nonlocal interactions, we here restrict ourselves to local ones. That is, in each unit cell  $i$ , the matrix  $U_{lm'l'm'}$  parameterizes scattering events in which local orbitals  $l, l', m, m'$  are involved. In cases where the unit cell contains multiple atoms, the matrix elements of  $U_{lm'l'm'}$  are nonzero only when all indices correspond to interacting orbitals of the same atom (i.e., are local interactions). This restriction can be relaxed, in principle, to include also nonlocal interactions within the unit cell, either defining the whole unit cell as “local” or including the bare nonlocal interactions within the (then nonlocal) vertex building block for ladder D $\Gamma$ A.

The physics of the Hubbard model is usually studied in the framework of the Green’s function formalism. Our computational methods additionally employ the Matsubara formalism, where the one-particle Green’s function for a system in thermal equilibrium at temperature  $T = 1/\beta$  is defined by

$$G_{lm}^k = - \int_0^\beta d\tau e^{i\nu\tau} \langle T_\tau \hat{c}_{\mathbf{k}l}(\tau) \hat{c}_{\mathbf{k}m}^\dagger(0) \rangle. \quad (2)$$

Here, the 4-index  $k = (i\nu, \mathbf{k})$  combines Matsubara frequency  $i\nu$  and crystal momentum  $\mathbf{k}$ ;  $\tau$  is the imaginary time. Spin in-

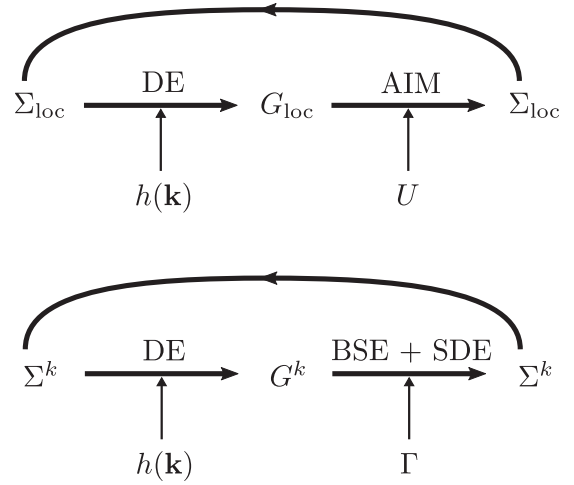


FIG. 1. Schematic explanation of DMFT and D $\Gamma$ A loops.

indices were omitted here, since we consider only paramagnetic systems with spin-diagonal Green’s functions. The interacting Green’s function contains (infinitely) many connected Feynman diagrams that are, via the Dyson equation (DE), captured by the self-energy:

$$\Sigma_{lm}^k = (i\nu + \mu)\delta_{lm} - h_{lm}(\mathbf{k}) - [G_{lm}^k]^{-1}. \quad (3)$$

### B. Dynamical mean-field theory

In most cases, it is completely infeasible to compute  $G_{lm}^k$  or  $\Sigma_{lm}^k$  directly through these infinitely many Feynman diagrams. Instead, one is bound to rely on approximations. In the DMFT approximation the self-energy is assumed to be strictly local or momentum independent. This becomes exact in infinite dimensions, while it still remains an excellent approximation in three dimensions and even for many two-dimensional systems. As we illustrate in Fig. 1 in a very abstract way, DMFT consists of two steps: First, one uses the  $\mathbf{k}$ -integrated Dyson equation (3) to obtain the local Green’s function from the local ( $\mathbf{k}$ -independent) DMFT self-energy:

$$G_{lm}^v = \frac{1}{V_{\text{BZ}}} \int_{\text{BZ}} d^d k [(i\nu + \mu)\delta_{lm} - h_{lm}(\mathbf{k}) - \Sigma_{lm}^v]^{-1}. \quad (4)$$

Here, the integral over the crystal momentum  $\mathbf{k}$  is taken over the first Brillouin zone (BZ) with volume  $V_{\text{BZ}} = (2\pi)^d/V$  ( $V$ : unit cell volume;  $d$ : dimension). The chemical potential  $\mu$  is chosen such that the system contains the desired number of electrons. In the second step one obtains a new local self-energy, which is in principle the sum of all self-energy diagrams built from the above propagator and the local interaction. These two steps can be iterated until convergence.

In practice the second step is usually solved by introducing an auxiliary Anderson impurity model (AIM), since a direct summation of all diagrams is infeasible. For the AIM, on the other hand, it is possible to calculate correlation functions like the one-particle Green’s function  $g_l^v$  on the impurity numerically exactly.

### C. Local correlations on the two-particle level

Despite the success of DMFT, additional efforts are necessary in order to access also the momentum dependence of the self-energy. There are several diagrammatic extensions of DMFT that result in the momentum dependent self-energy (for a review see Ref. [14]). These diagrammatic routes to nonlocal correlations all rely on two-particle vertices from DMFT. Here locality is assumed on the two-particle level, instead of the one-particle level. Local correlations on the two-particle level [44] are contained in the two-particle Green's function of the (DMFT) impurity model,

$$G_{abcd}^{\nu_1\nu_2\nu_3\nu_4} = \frac{1}{\beta^2} \int_0^\beta d\tau_1 d\tau_2 d\tau_3 d\tau_4 e^{i(\nu_1\tau_1 - \nu_2\tau_2 + \nu_3\tau_3 - \nu_4\tau_4)} \times \langle T_\tau \hat{c}_a(\tau_1) \hat{c}_b^\dagger(\tau_2) \hat{c}_c(\tau_3) \hat{c}_d^\dagger(\tau_4) \rangle, \quad (5)$$

for which we use spin-orbital compound indices  $a, b, c, d$ . In this paper we compute such two-particle Green's functions by continuous-time quantum Monte Carlo (CT-QMC) with worm sampling [45], which is implemented in W2DYNAMICS [46].

The two-particle Green's function is connected to the full reducible vertex  $F_{abcd}$  by

$$G_{abcd}^{\nu_1\nu_2\nu_3\nu_4} = g_a^{\nu_1} g_c^{\nu_3} (\delta_{12} - \delta_{14}) - \frac{1}{\beta} g_a^{\nu_1} g_b^{\nu_2} g_c^{\nu_3} g_d^{\nu_4} F_{abcd}^{\nu_1\nu_2\nu_3\nu_4}, \quad (6)$$

where  $\delta_{12} \equiv \delta_{ab}\delta_{cd}\delta_{\nu_1\nu_2}$  and  $\delta_{14} \equiv \delta_{ad}\delta_{bc}\delta_{\nu_1\nu_4}$ . Closely related is the generalized susceptibility

$$\begin{aligned} \chi_{abcd}^{\nu_1\nu_2\nu_3\nu_4} &= \beta (G_{abcd}^{\nu_1\nu_2\nu_3\nu_4} - g_a^{\nu_1} g_c^{\nu_3} \delta_{12}) \\ &\equiv \chi_{0,abcd}^{\nu_1\nu_2\nu_3\nu_4} + \chi_{\text{conn},abcd}^{\nu_1\nu_2\nu_3\nu_4}, \end{aligned} \quad (7)$$

with

$$\chi_{0,abcd}^{\nu_1\nu_2\nu_3\nu_4} = -\beta g_a^{\nu_1} g_c^{\nu_3} \delta_{14}. \quad (9)$$

Since energy conservation constrains  $\nu_1 + \nu_3 = \nu_2 + \nu_4$ , it is sometimes of advantage [47] to make a transition from four fermionic frequencies to a notation with two fermionic and one bosonic Matsubara frequency.

If we choose the bosonic frequency as  $\omega_{\text{ph}} = \nu_1 - \nu_2$ , the Bethe-Salpeter equation (BSE) in the particle-hole channel can be solved separately at each bosonic frequency. In the particle-particle channel, we have to choose  $\omega_{\text{pp}} = \nu_1 + \nu_3$  instead. Furthermore, the Bethe-Salpeter equations can be diagonalized in spin space by the following linear combinations:

$$F_{d,nlhm} = F_{n\uparrow l\uparrow h\uparrow m\uparrow} + F_{n\uparrow l\uparrow h\downarrow m\downarrow}, \quad (10)$$

$$F_{m,nlhm} = F_{n\uparrow l\uparrow h\uparrow m\uparrow} - F_{n\uparrow l\uparrow h\downarrow m\downarrow}, \quad (11)$$

$$F_{s,nlhm} = F_{n\uparrow l\uparrow h\uparrow m\uparrow} + F_{n\uparrow l\uparrow h\downarrow m\downarrow}, \quad (12)$$

$$F_{\downarrow,nlhm} = F_{n\uparrow l\uparrow h\uparrow m\uparrow} - F_{n\uparrow l\uparrow h\downarrow m\downarrow}. \quad (13)$$

The Bethe-Salpeter equations for the impurity in the particle-hole (ph) channel are thus

$$F_{r,lmml'}^{\nu\nu'\omega} = \Gamma_{r,lmml'}^{\nu\nu'\omega} + \sum_{\substack{m'h' \\ nu'}} \Gamma_{r,lmhn}^{\nu\nu''\omega} \chi_{0,nhh'n'}^{\nu''\nu'\omega} F_{r,n'h'm'l'}^{\nu''\nu'\omega}, \quad (14)$$

where  $r = d, m$  denotes the afore-defined channel and  $\omega \equiv \omega_{\text{ph}}$  is the bosonic frequency. For better readability we will

adopt the shorthand notation

$$F_r^\omega = \Gamma_r^\omega + \Gamma_r^\omega \chi_0^\omega F_r^\omega, \quad (15)$$

where all quantities are matrices in an orbital-frequency compound index.

### D. Dynamical vertex approximation

The D $\Gamma$ A is a diagrammatic extension of DMFT that assumes locality of the irreducible vertex, which is taken as input from an auxiliary impurity problem (usually from a converged DMFT solution to the original problem). Since its original formulation in Ref. [18], the D $\Gamma$ A was developed in three main directions (often called different D $\Gamma$ A flavors):

(i) the original parquet formulation (p-D $\Gamma$ A), where the locality is assumed on the level of the fully irreducible vertex  $\Lambda$ —this flavor treats the smallest set of diagrams as local, and correspondingly it is computationally most demanding [35,37];

(ii) ladder D $\Gamma$ A (in combination with DFT input also called *ab initio* D $\Gamma$ A [15–17]), where it is the irreducible vertex in the particle-hole channel ( $\Gamma_{\text{ph}}$ ) that is assumed local;

(iii)  $\lambda$ -corrected D $\Gamma$ A (usually also called ladder D $\Gamma$ A), where as in (ii) the irreducible vertex  $\Gamma_{\text{ph}}$  is taken as local. However, after the solution of the Bethe-Salpeter equations [a nonlocal version of Eq. (15)], a sum rule is imposed on the susceptibility by introducing the so-called Moriyasque  $\lambda$  correction [19,20,48] to the susceptibility and self-energy.

Below we first briefly review these three existing flavors, as this allows placing the new flavor (sc-D $\Gamma$ A; introduced in the next section) into its proper methodological context.

#### 1. Parquet D $\Gamma$ A

The parquet scheme is a method to self-consistently calculate one-particle and two-particle quantities [39–42] (it is closely related to the multiloop generalization [49,50] of the functional renormalization group (fRG) method [51]). Given a one-particle Green's function  $G$  and the fully two-particle irreducible [52] two-particle vertex  $\Lambda$ , one can iterate the parquet equation

$$F_r = \Lambda_r + \sum_{r'} c_{r'} \underbrace{\Gamma_{r'} \chi_0 F_{r'}}_{\Phi_{r'}} \quad (16)$$

and the lattice BSE

$$F_r^q = \Gamma_r^q + \Gamma_r^q \chi_0^q F_r^q \quad (17)$$

to obtain the (in general nonlocal) vertices  $F_r$  and  $\Gamma_r$ . Here the index  $r = d, m, s, t$  is as defined earlier the channel index,  $c_r$  denotes a real prefactor, and Eq. (17) is diagonal in the bosonic variable (four-index  $q$ ). In our short notation  $F_r^q$  and  $\Gamma_r^q$  are matrices in two fermionic multi-indices as before. The parquet equation Eq. (16) is not diagonal in the bosonic four-index and its evaluation requires evaluation of the per definition reducible vertices  $\Phi_r$  at different frequency and momentum combinations (for explicit formulation see, e.g., Ref. [35]).

The Green's function entering the above Eqs. (16) and (17) via  $\chi_0$  can also be updated, since the full vertex  $F$  is related to self-energy through the Schwinger-Dyson equation (SDE, see, e.g., Ref. [35]). The SDE together with the Dyson equation

and Eqs. (16) and (17) constitute a closed set with only one input quantity:  $\Lambda$ . For an exact  $\Lambda$ , the parquet scheme produces the exact one- and two-particle quantities. In practice, for example  $\Lambda = U$  is taken, which is the lowest order in perturbation expansion widely known as the parquet approximation [40,41]. In the parquet D $\Gamma$ A method  $\Lambda$  is assumed local and taken from a converged DMFT calculation [53].

*Truncated unity approximation.* The parquet scheme is numerically extremely costly [35]. We thus employ an additional approximation. Specifically, we transform the fermionic momentum dependence of the two-particle reducible vertices  $\Phi_r$  into a real space basis, leaving only the bosonic momentum  $\mathbf{q}$ :

$$\tilde{\Phi}_r^{\ell\ell'q} = \frac{1}{N} \sum_{k,k'} (f^{k\ell})^* \Phi_r^{kk'q} f^{k'\ell'}, \quad (18)$$

where  $f^{k\ell}$  are basis functions (typically known as form factors) of a suitable transformation-matrix which we choose to obey certain symmetries. Exploiting the relative locality [37,54] of the reducible vertices  $\Phi$  in their two fermionic momenta we limit the number of basis functions  $f^{k\ell}$  used for the transformation (hence the name *truncated unity*). This amounts to setting the more nonlocal parts (in the fermionic arguments) of the two-particle reducible vertices to zero.

$$\tilde{\Phi}_r^{\ell\ell'q} = 0 \quad \text{for } \ell, \ell' > l_{\max} \quad (19)$$

The calculations to transform the entire parquet scheme including convergence studies in the number of basis functions can be found in Refs. [37,55]. The truncated unity implementation (TUPS) [37] with one or nine form factors was used to generate the comparison data in Sec. IV.

## 2. Ladder D $\Gamma$ A

Even with the truncated unity approximation the parquet D $\Gamma$ A is numerically very costly. It also suffers from the presence of divergencies [56–60] in the fully irreducible vertex  $\Lambda$  that is directly taken as input. Therefore it is often preferable to use ladder D $\Gamma$ A, where the locality level is raised to the irreducible vertex in the particle-hole channel  $\Gamma_{d/m,\text{imp}}$ . The choice of channel is here determined by the dominant type of nonlocal fluctuations. By choosing the particle-hole channel we take nonlocal magnetic and density fluctuations into account, while treating particle-particle fluctuations only at the local level [61]. Note that the transversal particle-hole fluctuations will later be included on the same level by using the crossing symmetry, which relates it to the particle-hole channel.

Then, D $\Gamma$ A becomes significantly simpler and essentially consists of two steps: First one has to compute the Bethe-Salpeter equations

$$F_r^q = [1 - \Gamma_{r,\text{imp}}^\omega \chi_0^q]^{-1} \Gamma_{r,\text{imp}}^\omega \quad (20)$$

in the particle-hole channels  $r = d, m$ . Since the irreducible impurity vertices  $\Gamma_{r,\text{imp}}$  can also exhibit divergences, it is better to reformulate the above equation. This is done by expressing  $\Gamma$  by Eq. (15) and rearranging the terms, as shown in Ref. [15]. Then one arrives at

$$F_r^q = F_r^\omega [1 - \chi_0^{\text{nl},q} F_r^\omega]^{-1} \quad (21)$$

containing only the full reducible vertex  $F$ , and the nonlocal part of the bubble  $\chi_0^{\text{nl},q} = \chi_0^q - \chi_0^\omega$ .

The momentum-dependent reducible vertices  $F_r^q$  from the longitudinal and transversal particle-hole channels are then combined. We do not need to calculate the latter explicitly, because it can be obtained from the former through the crossing symmetry [14]. The combined vertex  $\mathcal{F}$  is then

$$\begin{aligned} \mathcal{F}_{d,\text{nl}hm}^{kk'q} &= F_{d,\text{nl}hm}^{\text{vv}'\omega} + F_{d,\text{nl}hm}^{\text{nl},\text{vv}'q} \\ &\quad - \frac{1}{2} F_{d,\text{hl}nm}^{\text{nl},(\text{v}'-\omega)\text{v}'(k'-k)} - \frac{3}{2} F_{m,\text{hl}nm}^{\text{nl},(\text{v}'-\omega)\text{v}'(k'-k)} \end{aligned} \quad (22)$$

(see also Eq. (54) in Ref. [15]). Vertices labeled “nl” are nonlocal, i.e.,  $F_{r,\text{nl}hm}^{\text{nl},\text{vv}'q} = F_{r,\text{nl}hm}^{\text{vv}'q} - F_{r,\text{nl}hm}^{\text{vv}'\omega}$ . Inserting this into the Schwinger-Dyson equation of motion [15]

$$\Sigma_{mm'}^{\text{con},k} = -\frac{1}{\beta} \sum_{\text{nl}hm'l'h'} \sum_{k'q} U_{\text{ml}hn} \chi_{0,\text{nl}l'n'}^{k'k'q} \mathcal{F}_{d,n'l'h'm'}^{kk'q} G_{hh'}^{k-q} \quad (23)$$

yields the connected part of the momentum-dependent self-energy. In practice this equation is evaluated separately for the summands of  $\mathcal{F}$  in Eq. (22) [17], such that one can identify the nonlocal corrections to the DMFT self-energy.

Equations (21)–(23) can be evaluated efficiently even for multiorbital models with  $h(\mathbf{k})$  from DFT as input. This is known as the *ab initio* D $\Gamma$ A [15–17]. Hitherto they are evaluated only once, and this flavor is therefore referred to as one-shot D $\Gamma$ A (1-D $\Gamma$ A) in the following.

## 3. $\lambda$ -corrected D $\Gamma$ A

The self-energy obtained in the one-shot ladder-D $\Gamma$ A calculation does not always exhibit the correct asymptotic behavior, especially if the susceptibility is large. In addition, the susceptibilities related to Eq. (21) diverge at the DMFT Néel temperature, violating the Mermin-Wagner theorem [62] for two-dimensional models. This problem was partially solved by so-called  $\lambda$  corrections [19,20], where one enforces the sum rule for the spin (or spin and charge) susceptibility(-ies) by adapting a parameter  $\lambda$  (hence the name).

While very successful for one-band models [22–25,48,63], this solution is not straightforwardly extensible to multiorbital systems. The reasons are twofold. Firstly,  $\lambda$  would be a matrix with as many independent entries as there are different spin-orbital combinations, resulting in a multidimensional optimization problem. Secondly, the solution to this problem is quite likely nonunique and there are at the moment no criteria how the physical matrix  $\lambda$  should be chosen. While we do not exclude that a reasonable scheme can be devised for the multiorbital case in the future (see, e.g., [64,65] for application of sum rules in the multiorbital two-particle self-consistent approach [66]), we focus here on an alternative scheme that does not rely on enforcing sum rules.

## III. SELF-CONSISTENT LADDER D $\Gamma$ A

While the  $\lambda$  correction is impractical or perhaps not even possible for multiorbital systems, a one-shot ladder-D $\Gamma$ A calculation as hitherto employed for realistic materials calculations also has severe limits. Where the nonlocal corrections become strong, its application is not justified. When

the DMFT susceptibility diverges at a phase transition, the nonlocal corrections of a one-shot D $\Gamma$ A calculation are not meaningful any more.

There are two main physical reasons why this is wrong: Firstly, the ladder diagrams of say the particle-hole channel lack insertions from the particle-particle channel, which dampen the particle-hole fluctuations. These diagrams are taken into account only on the level of the impurity. In order to correctly incorporate the nonlocal contributions to such insertions, we need to evaluate the full parquet scheme that is at the moment numerically too costly for multiorbital calculations.

Secondly and arguably even more important, the self-energy that enters the propagators in the BSE is still the local DMFT self-energy in a one-shot D $\Gamma$ A. This DMFT self-energy fulfills the local SDE with local  $F^\omega$ , where the nonlocal contributions do not enter. By using the updated nonlocal self-energy in the BSE, we can introduce feedback from two-particle nonlocal correlations to the one-particle quantities. For example, spin fluctuations lead to a reduced lifetime which, when included in the ladder Green's function or self-energy, reduces the spin fluctuations in turn. This mechanism hence suppresses the magnetic transition temperature below the DMFT mean-field value.

### A. sc D $\Gamma$ A

The approach we propose here consists of finding a momentum-dependent self-energy for a lattice, defined by the tight-binding Hamiltonian  $h(\mathbf{k})$ , that is consistent with the local irreducible vertex  $\Gamma_{\text{ph,imp}}$ . This can be achieved by using an iterative scheme illustrated in the lower panel of Fig. 1 in order to underline its formal similarity to DMFT: The first step is again the construction of propagators by the DE [Eq. (3)], with a chemical potential that constrains the electron number. But in contrast to DMFT the self-energy is now momentum dependent. In the second step we sum up all self-energy diagrams that are generated from the local vertex  $\Gamma$ . More explicitly, this step consists of the subsequent evaluation of the BSE [Eq. (21)] and SDE [Eq. (23)]. Just as in DMFT, here the second step is numerically much more expensive than the first (DE) step.

The self-energy resulting from the first iteration of ladder D $\Gamma$ A is taken to be the input (or ‘‘trial’’) for the second iteration. Starting from the third iteration, linear combinations of trial and result self-energies from several previous iterations are used as new trials. The linear combination is constructed by the Anderson acceleration algorithm [67,68]; see also Appendix A. If the result is equal to the trial, the iteration is stopped. The workflow of such a calculation is illustrated in Fig. 2.

To our knowledge there is no proof of uniqueness or existence of such a fixed point. However, we find the procedure to be convergent over a large range of parameters (cf. Fig. 3 which is discussed in Sec. IV).

In case of convergence, the asymptotic behavior of the self-energy is largely repaired with respect to one-shot D $\Gamma$ A calculations. Furthermore, the magnetic susceptibility in two-dimensional models stays finite at all temperatures in agreement with the Mermin-Wagner theorem.

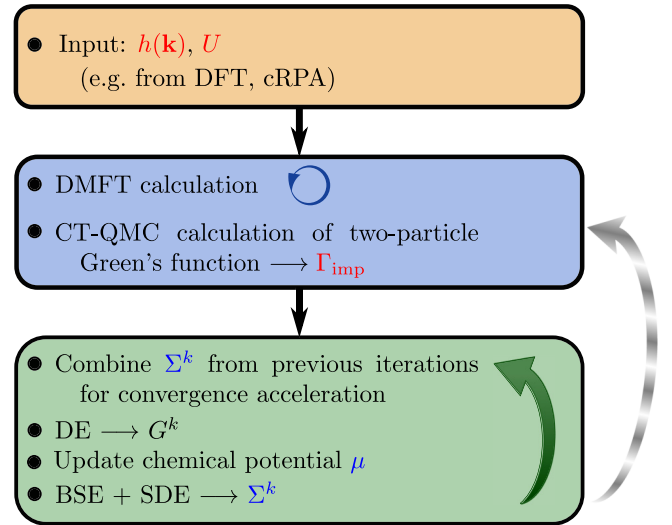


FIG. 2. Step-by-step illustration of a self-consistent ladder D $\Gamma$ A calculation. The first box (orange color) shows preliminary calculations to set up the model. The second box (blue color) concerns the DMFT calculations, and the third one (green color) shows the sc-D $\Gamma$ A cycle. Quantities written in red are kept constant throughout the whole calculation; those in blue are self-consistently determined in sc-D $\Gamma$ A.

### B. Implementation and computational effort

The sc-D $\Gamma$ A is applicable to multiorbital calculations using the AbinitioD $\Gamma$ A code [17], with the slight modification of allowing for momentum-dependent self-energies in the input. A step-by-step description of the workflow is given in Fig. 2, whereas in Appendix A we provide more technical details of how this is done in operation with the AbinitioD $\Gamma$ A.

The first step (orange box in Fig. 2) is the creation of a model. It can be based on *ab initio* calculations and consists

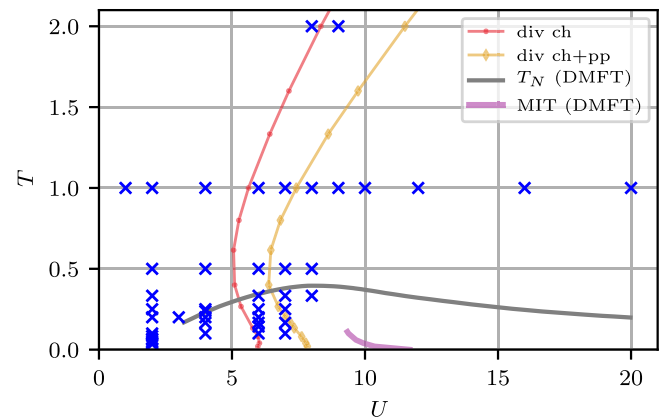


FIG. 3. Phase diagram of the square-lattice Hubbard model at half filling. Blue crosses denote points at which the sc-D $\Gamma$ A could be converged. The DMFT-Néel temperature is shown in gray (from Ref. [73]). The magenta line indicates the DMFT metal-insulator transition. We also show the first two vertex divergence lines (from Ref. [56]).

of a tight-binding Hamiltonian as well as a parametrization of the interaction in the form of a  $U$  matrix.

The second step is to determine a local (impurity) vertex  $\Gamma_{\text{imp}}$ . Here, this is obtained from the local impurity problem at DMFT self-consistency as indicated in the blue box in Fig. 2; then usually the DMFT self-energy is also taken as a starting point for the following D $\Gamma$ A calculations. It is however not strictly required to start from a converged DMFT calculation. One might as well start from  $GW$  or calculate  $\Gamma_{\text{imp}}$  from the D $\Gamma$ A Green's function in an additional self-consistency step, as indicated by the dashed gray arrow in Fig. 2 but not done in this paper.

Finally, the actual sc-D $\Gamma$ A cycle is illustrated in the green box of Fig. 2. It essentially amounts to the execution of the AbinitioD $\Gamma$ A code [17], but in the repeated evaluation of Eqs. (21)–(23), we have to generate updated input quantities after every iteration, until convergence is reached. Here, also the chemical potential  $\mu$  is adjusted so that the total number of electrons is kept fixed.

In the sc-D $\Gamma$ A implementation the local irreducible vertex is never used explicitly, and the equations are evaluated in terms of the local full vertex  $F^\omega$  [Eq. (21) instead of Eq. (20)]. As already mentioned, this avoids the computational difficulties coming from using a very large irreducible vertex near or on a divergence line. Indeed, the sc-D $\Gamma$ A scheme can be converged also quite close to the divergence lines (cf. Fig. 3). Let us however note that the local part of self-energy in the converged sc-D $\Gamma$ A calculation is in general not related to  $F^\omega$  via the local SDE (as it was the case in a one-shot ladder D $\Gamma$ A). The sc-D $\Gamma$ A corrections to the self-energy modify thus also its local part that is not any more equal to the DMFT solution. One can envisage [14,15,69] an update of the local multiorbital vertex  $\Gamma$  (dashed gray arrow in Fig. 2; not implemented here) so that the local Green's function of the impurity is equal to the local sc-D $\Gamma$ A Green's function. Such an update is at the moment numerically prohibitively expensive and hence beyond our scope.

At this point, it is appropriate to comment on the computational effort of the present self-consistent ladder D $\Gamma$ A. The cost of a DMFT calculation and the two-particle Green's function depends mainly on the desired accuracy, if one is using a Monte Carlo method as an impurity solver. The scaling of the CT-QMC with temperature and number of orbitals has been discussed in the literature [13]. The measurement of the two-particle Green's function in worm sampling of w2dynamics scales as  $\sim(\#\omega)^3 M_{\text{comp}}$ , where  $M_{\text{comp}}$  is the number of non-vanishing spin-orbital components. In the case of Kanamori interaction this goes as  $M_{\text{comp}} \sim M^2$ , where  $M$  is the number of impurity orbitals [70]. For a general dense  $U$  matrix, the number of components is  $M_{\text{comp}} = (2M)^4$ . The number of frequencies  $\#\omega$  has to be scaled linearly with  $1/T$  as lower temperatures are approached. Note that at this point we do not distinguish between the number of fermionic and bosonic frequencies, since at least their scaling with temperature is the same.

Having calculated the two-particle Green's function, the remaining time of the computation is direct proportional to the number of iterations ( $N_{\text{iter}}$ ) needed for convergence.  $N_{\text{iter}}$  ranges from a few ( $\sim 10$ ) at high-temperatures to many ( $\sim 200$ ) iterations at low temperatures. However, in problems with

TABLE I. Computational effort [time measured in core hours (h) on an Intel Skylake Platinum 8174 processor with 3.1 GHz] for the calculation of the local two-particle vertex  $\Gamma_{\text{imp}}$  (blue box in Fig. 2) and the sc-D $\Gamma$ A (green box in Fig. 2) for a few cases treated in this paper. ‘‘Sq. latt.’’ (square lattice) refers to Sec. IV, ‘‘2-band’’ refers to the two-band model treated in Sec. V.

Case	[Time] $_{\Gamma_{\text{imp}}}$	[Time] $_{\text{sc-D}\Gamma\text{A}}$
Sq. latt., $U = 2, 1/T = 4$	2400 h	65 h
Sq. latt., $U = 2, 1/T = 20$	43 000 h	11 000 h
2-band, $1/T = 10$	13 000 h	3000 h
2-band, $1/T = 20$	40 000 h	70 000 h

weak spin fluctuations,  $N_{\text{iter}}$  is hardly dependent on temperature. In our experience, convergence is accelerated if the DMFT self-energy  $\Sigma$  used as a starting point has little noise. Therefore we use symmetric improved estimators [71] to compute it in CT-QMC. Noise in the vertex, on the other hand, does not have a large influence on the self-energy in D $\Gamma$ A, as shown recently [72].

The computational effort of one D $\Gamma$ A iteration has been discussed in Ref. [17]. Let us give a brief overview for the sake of completeness. In this part, most time has to be spent with the BSE, where it is necessary to ( $\#\omega\#\mathbf{q}$ ) times invert a matrix of dimension ( $M^2\#\omega$ ). Overall this gives a scaling of  $\sim\#\mathbf{q}(\#\omega)^{3.5}M^5$  [17].

In order to give a rough feeling or rule of thumb for the computational cost, we remark that at high temperatures the DMFT and CT-QMC calculations take considerably more time than the D $\Gamma$ A self-consistency cycle. For the most complicated cases, where many iterations are needed for convergence, one may expect to spend about twice as much time for ladder D $\Gamma$ A than for the CT-QMC. We illustrate this by providing the actual CPU hours that were spent on some of the calculations in Table I.

### C. Relation to p-D $\Gamma$ A

The self-consistency imposed on the self-energy that is obtained by iterative application of BSE (21), crossing symmetry (22), and SDE (23) is reminiscent of the parquet scheme. The main difference is the lack of the full parquet equation (16), which would include also nonlocal particle-particle insertions in the full vertex  $F$ . In the full p-D $\Gamma$ A the level of local approximation is also different, since  $\Lambda$  contains fewer diagrams than  $\Gamma$ . In the truncated unity approximation however,  $\Gamma$  is also effectively local if we do calculations with only one form factor (1FF p-D $\Gamma$ A). It can be explicitly seen, e.g., in Eq. (21) in Ref. [37]. The difference between the irreducible vertices  $\Gamma$  in the two approaches is that in sc-D $\Gamma$ A it is taken from DMFT and never updated during the self-consistency cycle, whereas in 1FF p-D $\Gamma$ A it is updated through the parquet equation in every iteration. This update allows for mixing of scattering channels in 1FF p-D $\Gamma$ A, notwithstanding the fact that the nonlocal contributions from other channels into  $\Gamma$  are averaged over momenta.

#### IV. SQUARE LATTICE HUBBARD MODEL

We begin the application of the sc-D $\Gamma$ A method by considering a relatively simple system, which already has been studied well in some parameter regimes: the one-orbital Hubbard model on a square lattice with nearest-neighbor hopping. The dispersion  $h(\mathbf{k})$  in Eq. (1) is then simply

$$h(\mathbf{k}) = -2(\cos(k_x) + \cos(k_y)), \quad (24)$$

where the nearest-neighbor hopping amplitude is set to  $t \equiv 1$  to define our unit of energy for this section (with  $\hbar \equiv 1$  setting the frequency unit). Furthermore, the lattice constant  $a \equiv 1$  sets the unit of length and  $k_B \equiv 1$  the unit of temperature, and the orbital indices  $l, m, l', m'$  are restricted to a single orbital at each site.

In Fig. 3 we show the DMFT phase diagram of the Hubbard model on a square lattice at half filling ( $n = 1$  electron per site). With blue crosses we denote points in the phase diagram for which we were able to obtain a converged sc-D $\Gamma$ A solution. Please note that the sc-D $\Gamma$ A method can be used both below the DMFT Néel temperature (indicated by the gray curve in Fig. 3) as well as between the divergence lines (red and orange curves in Fig. 3). It is only on or directly next to divergence lines that we were not able to obtain convergence.

The phase diagram in Fig. 3 serves as a proof of principle and it is not our intention to discuss the sc-D $\Gamma$ A results in the different parameter regimes in the current paper. Instead, we show selected results for weak ( $U = 2$ ) and intermediate ( $U = 4$ ) coupling, where comparison to other methods is possible, as well as for strong coupling ( $U = 8$ ) and out of half filling ( $n = 0.85$ ) to show the applicability of the method in this interesting (e.g., with regard to superconductivity) regime.

##### A. Weak coupling

In order to benchmark the method against known results, we first study a half-filled weak coupling case, with the interaction  $U = 2$  (in our units the bandwidth is  $W = 8$ ). This case was intensively studied by various methods in Ref. [63], and in the spirit of Ref. [63] we focus on spin fluctuations and the formation of the pseudogap at low temperature.

In Fig. 4 the static magnetic susceptibility at  $\mathbf{q} = (\pi, \pi)$  is shown. For  $U = 2$  DMFT predicts a phase transition at  $T_N \approx 0.08$ . The sc-D $\Gamma$ A leads to a seemingly nondiverging antiferromagnetic (AFM) susceptibility; the updated self-energy in the BSE dampens the magnetic fluctuations and removes the divergence. In the temperature range accessible, the sc-D $\Gamma$ A susceptibility shows first a  $1/(T - T_N)$  behavior, as in DMFT which has a finite Néel temperature  $T_N$ , and then deviates to a linear behavior on the log scale of Fig. 4, corresponding to  $\chi_m(T) \sim \exp(\alpha/T)$  with some constant  $\alpha$ . Such an exponential scaling with a divergence only at  $T = 0$  is to be expected for a two-dimensional system, fulfilling the Mermin-Wagner theorem [62] (cf. also Fig. 13 in Ref. [63]).

The sc-D $\Gamma$ A AFM susceptibility is somewhat smaller than the one from  $\lambda$ -corrected D $\Gamma$ A presented in Ref. [63] (not shown here) as well as slightly smaller than the parquet-D $\Gamma$ A results (shown in Fig. 4 for one and nine form factors). The overall behavior is however well reproduced.

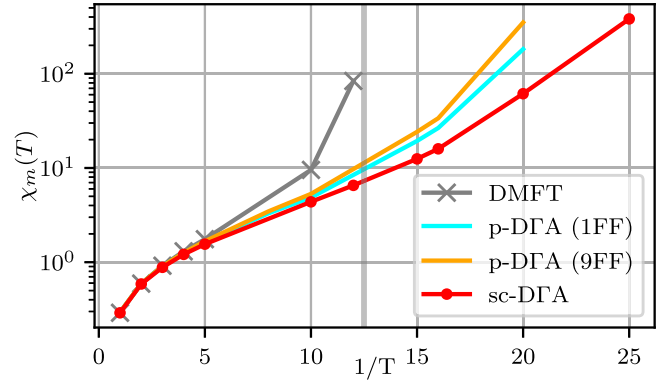


FIG. 4. Static magnetic susceptibility of the square-lattice Hubbard model with  $U = 2$  and  $n = 1$  at momentum  $\mathbf{q} = (\pi, \pi)$  as a function of inverse temperature. Different colors and symbols denote different methods. The gray vertical line marks the DMFT Néel temperature.

In order to correctly resolve the growing correlation length when lowering the temperature, the size of the momentum grid has to be increased. For the lowest two temperatures shown in Fig. 4 we performed extrapolation to infinite grid size (for details see Appendix B).

With lowering the temperature the growing spin fluctuations lead to enhanced scattering and suppression of the one-particle spectral weight at the Fermi energy and to opening of a pseudogap [19,63,76–79]. Due to the van Hove singularity [80–83] at the antinodal point  $\mathbf{k}_{AN} = (\pi, 0)$ , the suppression happens earlier (upon lowering  $T$ ) at this point than at the nodal point  $\mathbf{k}_N = (\pi/2, \pi/2)$ . In Fig. 5 we show the spectral functions (right) as well as the corresponding self-energies on the imaginary (Matsubara) frequency axis (left) for the two momenta  $\mathbf{k}_N$  and  $\mathbf{k}_{AN}$  and for different temperatures.

The pseudogap behavior of the spectral function is also visible in the imaginary part of self-energy on the Matsubara frequency axis. Upon lowering the temperature we first see metallic behavior at both nodal and antinodal points:  $|\text{Im}\Sigma_N|$  at the first Matsubara frequency is smaller than at the second. At lower temperatures, the slope of  $\text{Im}\Sigma_N$  at the first two Matsubara frequencies changes sign; first only at the antinodal point (pseudogap) and finally at both nodal and antinodal points. This is usually taken as a criterion for the opening of a pseudogap.

Note however that for  $1/T = 25$  there is already a pseudogap for  $\mathbf{k}_N$  in Fig. 5 (top right) while the slope of  $\text{Im}\Sigma_N$  is still negative in Fig. 5 (top left). However, a kink is visible. This kink of the analytic  $\Sigma_N$  function is apparently already enough for the analytic continuation to yield a large negative  $\text{Im}\Sigma_N$  at low real frequencies, which is needed for seeing a pseudogap.

In Fig. 6 we show the behavior of the imaginary part of the self-energy at the first three Matsubara frequencies for the nodal and antinodal points as a function of inverse temperature. Here we compare the sc-D $\Gamma$ A to parquet D $\Gamma$ A and  $\lambda$ -corrected ladder D $\Gamma$ A [63], and the diagrammatic quantum Monte Carlo (DiagMC) [63,84]. For the first Matsubara frequency all the methods lie almost on top of each other down to approx.  $1/T = 10$  (at the nodal point differences already

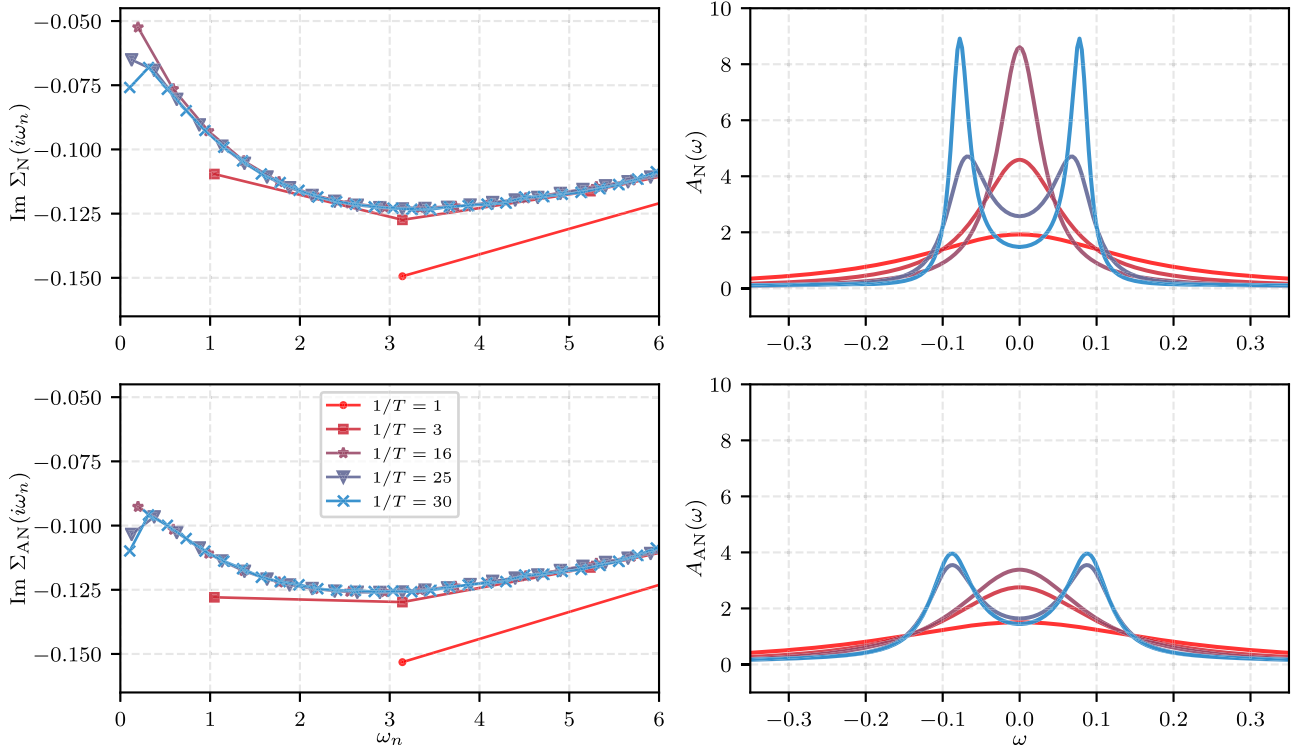


FIG. 5. The imaginary part of sc-DGA self-energy (left) and the corresponding spectral function (right) at  $U = 2$  and half filling for two momenta on the Fermi surface: nodal point,  $\mathbf{k}_N = (\pi/2, \pi/2)$ , and antinodal point,  $\mathbf{k}_{AN} = (\pi, 0)$ . Different colors and symbols denote different temperatures. The spectral functions were obtained by analytic continuation with the maximum entropy method [74,75].

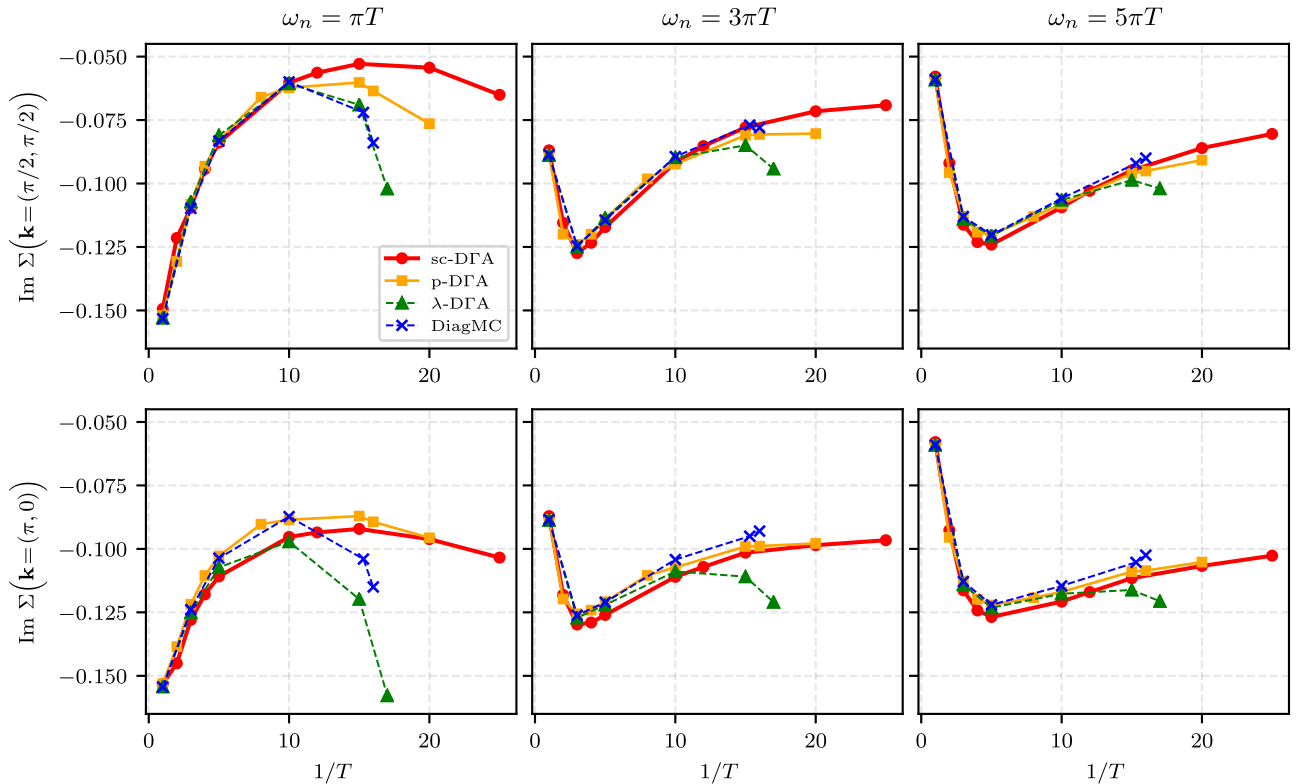


FIG. 6. Inverse temperature dependence of the imaginary part of self-energy at  $U = 2$  and half filling for the first three Matsubara frequencies  $\omega_n = \{\pi T, 3\pi T, 5\pi T\}$  for two momenta on the Fermi surface:  $\mathbf{k}_N = (\pi/2, \pi/2)$  and  $\mathbf{k}_{AN} = (\pi, 0)$ . Different colors and symbols denote different methods. The  $\lambda$ -DGA and DiagMC data in this figure were kindly provided by the authors of Ref. [63].



become noticeable at  $1/T = 10$ ). For lower temperatures the methods still qualitatively agree, but  $|\text{Im}\Sigma(\omega_n = \pi T)|$  grows faster in the  $\lambda$ -D $\Gamma$ A and quantitatively agrees better with the DiagMC benchmark. In the sc-D $\Gamma$ A, as well as in the p-D $\Gamma$ A, this growth happens at lower temperatures. This is in correspondence to the behavior of AFM susceptibility, which also grows slower in these methods upon lowering the temperature compared to  $\lambda$ -D $\Gamma$ A and DiagMC, while correctly reproducing the overall behavior.

If we however look at the two larger frequencies (middle and right panel of Fig. 6), the situation is opposite. Here both the p-D $\Gamma$ A as well as sc-D $\Gamma$ A follow the DiagMC benchmark closely up to  $1/T = 15$  and do not show any enhancement in  $|\text{Im}\Sigma|$  with lowering  $T$ , while in the  $\lambda$ -D $\Gamma$ A the second and third Matsubara frequency follow the behavior of the first one. This is probably a consequence of the  $\lambda$  correction that is applied *a posteriori* to the self-energy. While it works very well for the AFM susceptibility and it gives the correct behavior for the low energy part in the self-energy that is closely influenced (enhanced) by the strong spin fluctuations, it overestimates this influence for larger energies.

All in all, the comparison with the DiagMC benchmark shows the ability of sc-D $\Gamma$ A to describe the behavior of self-energy in all different temperature regimes: incoherent behavior at high temperatures, metallicity in the intermediate temperature regime, and the opening of spin-fluctuation induced pseudogap. Quantitatively the agreement with DiagMC is excellent down to approx.  $1/T = 10$ , with small quantitative differences visible for the lowest temperatures. The most pronounced difference is that the opening of the pseudogap is shifted to lower temperature than in DiagMC.

### B. Intermediate coupling

Next, we increase the interaction to  $U = 4$  but stay at half filling. Since we already enter a regime, where the numerically exact methods are limited to high temperatures, we do not show comparisons to benchmarks. We focus here on the comparison to parquet D $\Gamma$ A and the  $\lambda$ -corrected D $\Gamma$ A.

In Fig. 7 we show the static magnetic susceptibility as a function of momentum  $\mathbf{q}$  for two temperatures. We choose  $T = 0.25$  for also comparing with the DMFT result that diverges for slightly lower temperature. Already for  $T = 0.25$  we see a large difference from the DMFT result. As for the different D $\Gamma$ A methods, the results fall almost on top of each other with the exception of 1FF p-D $\Gamma$ A, where the susceptibility is somewhat larger close to the  $M$  point. For the lower temperature of  $T = 0.1$  the situation is quite different. Although all methods agree for momenta far from  $\mathbf{q} = (\pi, \pi)$ , close to it the results differ significantly, as was the case for  $U = 2$ . The sc-D $\Gamma$ A susceptibility is again the smallest, followed by the p-D $\Gamma$ A results.

In Fig. 8 we show the imaginary part of self-energy as a function of Matsubara frequency for the same two temperatures as in Fig. 7. For  $T = 0.25$  the D $\Gamma$ A methods agree well, although not any more quantitatively as it was in the weak-coupling case for this temperature. Here the 1FF p-D $\Gamma$ A result is noticeably different: At  $U = 4$  the 1FF approximation is not sufficient any longer at this temperature (cf. Ref. [37]). For  $T = 0.1$  at the antinodal point we already start to see the

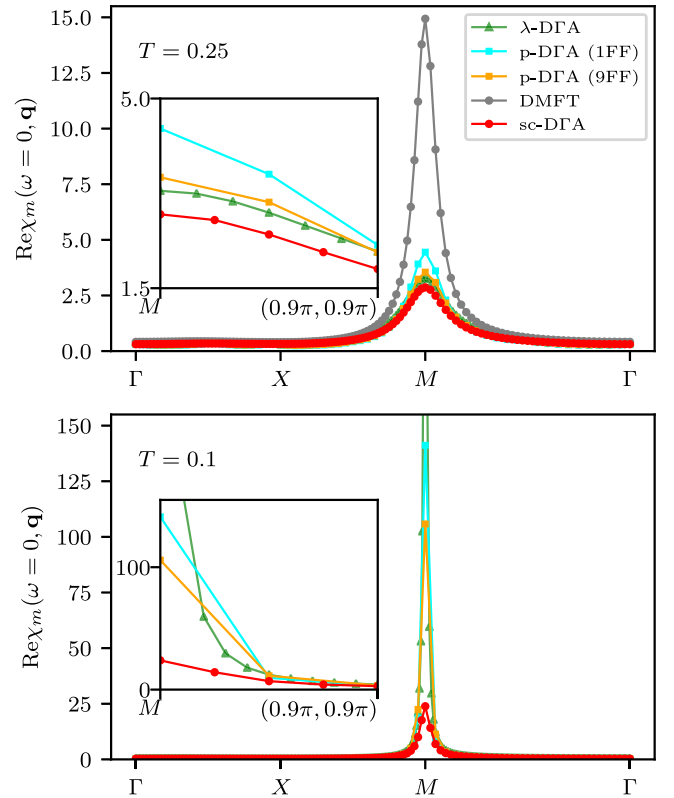


FIG. 7. Static magnetic susceptibility for  $U = 4$  on a path through the Brillouin zone for  $T = 0.25$  and  $T = 0.1$ . The value of  $\lambda$ -D $\Gamma$ A susceptibility at the  $M$  point is  $\chi_m(\omega = 0, \mathbf{q} = (\pi, \pi)) = 415$  (beyond the y range of the plot). A smaller momentum window is shown in the insets.

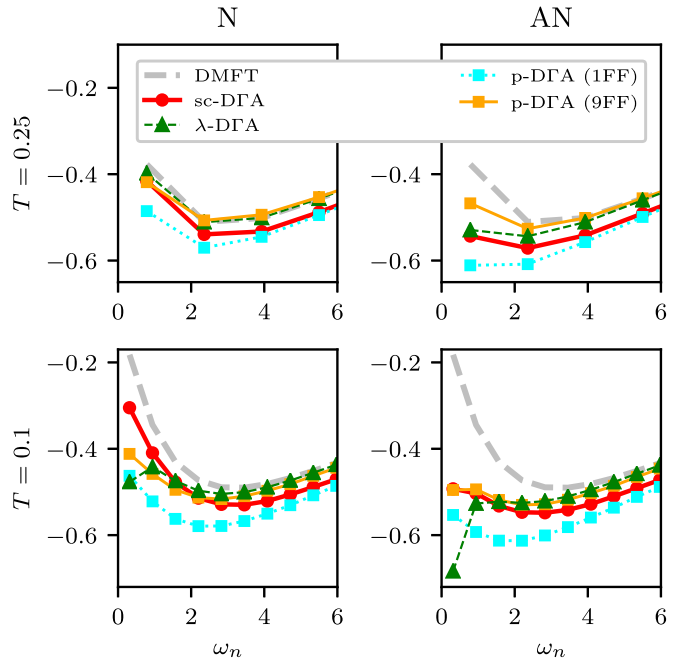


FIG. 8. Imaginary part of self-energy for the nodal (N) and antinodal (AN) points as a function of Matsubara frequencies for  $U = 4$ ,  $n = 1$  and two temperatures:  $T = 0.25$  and  $T = 0.1$ . Different methods are distinguished by different symbols and colors. The 1FF and 9FF p-D $\Gamma$ A data are reproduced from Ref. [37].

pseudogap behavior of self-energy in the sc-D $\Gamma$ A and p-D $\Gamma$ A methods, whereas in  $\lambda$ -D $\Gamma$ A the pseudogap sets in at a higher temperature of  $T \approx 0.17$  [48]. Except for the first Matsubara frequency, the three D $\Gamma$ A methods are in excellent, almost quantitative agreement. As in the  $U = 2$  case, the difference in the first Matsubara frequency is likely to be caused by much smaller AFM susceptibility in sc-D $\Gamma$ A as compared to  $\lambda$ -D $\Gamma$ A.

An open question remains why the sc-D $\Gamma$ A produces sizably smaller AFM susceptibility than the  $\lambda$ -D $\Gamma$ A upon going to low temperatures. For the case of  $U = 2$  it is also significantly smaller than the DiagMC result [63]. An intuitive partial understanding can be gained by looking at the p-D $\Gamma$ A results for one and nine form factors (1FF and 9FF). As already mentioned in Sec. III C and explained in Ref. [37], for the 1FF approximation to p-D $\Gamma$ A the irreducible vertex  $\Gamma$  is also local. But contrary to sc-D $\Gamma$ A, it is updated after each update of the self-energy. Therefore when the damping effect of self-energy at low temperature becomes big, it can be counterbalanced by a larger  $\Gamma$  which results in a larger susceptibility (cf. Figs. 4 and 7). In sc-D $\Gamma$ A this vertex stays the same throughout the calculation; the two-particle feedback onto the self-energy is reduced [85]. There is also no feedback from the particle-particle channel that is present in p-D $\Gamma$ A.

In the truncated unity p-D $\Gamma$ A we can make  $\Gamma$  systematically less local by using more form factors. It has also a strong effect on the susceptibility, as the 9FF p-D $\Gamma$ A results show. In the case of  $U = 2$  the susceptibility is larger for 9FF; it is, however, smaller than the 1FF result for  $U = 4$  (cf. Fig. 7). Similar (opposite) tendencies of the AFM susceptibility were seen for the two values of  $U$  in Ref. [37]. Although the convergence study in Ref. [37] shows that at  $T = 0.25$  the 9FF p-D $\Gamma$ A result is converged with respect to the number of form factors, it is quite likely not the case for much lower temperatures.

In the  $\lambda$ -corrected D $\Gamma$ A the vertex is also local and not updated. The imposed sum rule however imitates the mutual feedback of the one- and two-particle quantities.

### C. Strong coupling

Another interesting parameter regime that we can use the sc-D $\Gamma$ A method for is the doped strong-coupling case, which is relevant for superconductivity, as shown, e.g., in Refs. [24,25,86–90]. Going to sufficiently low temperatures, such as in the case of  $\lambda$ -D $\Gamma$ A [24,25], is a highly non-trivial task that requires computations with high numerical efficiency, since the momentum and frequency grids have to be sufficient to capture the growing correlation length.

In the following we show results for the Hubbard model on a square lattice with  $U = 8$  and 15% hole doping ( $n = 0.85$ ) in the temperature range  $T \in [0.05, 0.5]$ . With lowering the temperature the magnetic fluctuations, still antiferromagnetic at  $T = 0.5$ , become incommensurate. This is indicated by the shift of the maximum of the static magnetic susceptibility from  $\mathbf{q} = (\pi, \pi)$  to  $\mathbf{q} = (3\pi/4, \pi)$  in Fig. 9. If we look at the dynamic susceptibility  $\chi_m(\omega, \mathbf{q})$  at finite frequencies  $\omega$ , we can identify a splitting of the peak maximum. In the left panel of Fig. 10 we show the dynamic magnetic structure

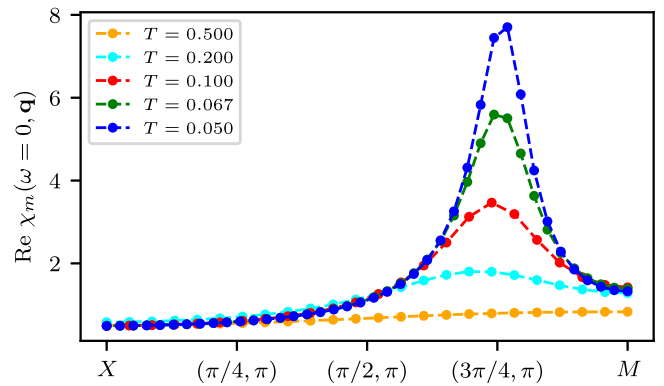


FIG. 9. Static magnetic susceptibility in sc-D $\Gamma$ A along the  $X$ - $M$  path in the Brillouin zone ( $q_y = \pi$ ) for different temperatures  $T$ ,  $U = 8t$ , and  $n = 0.85$ .

factor  $\text{Im}\chi_m(\mathbf{q}, \omega)/(1 - e^{-\omega/T})$ , obtained by analytic continuation with the maximum entropy method [74,75] for  $T = 0.05$  and also the position  $\omega_{\text{max}}$  of the maximum (or maxima) as a function of  $\mathbf{q}$  for different temperatures. The plots form characteristic  $Y$ -shaped spin-excitation dispersions, also seen experimentally [91] and discussed in Ref. [90]. We observe that the frequency  $\omega_{\text{max}}$ , at which the splitting occurs, moves to lower values as the temperature is lowered. It could be interpreted as sharpening of the dispersion relation upon lowering the temperature.

In the right panels of Fig. 11 the corresponding self-energy for the lowest temperature in Fig. 9,  $T = 0.05$ , is shown. The imaginary part becomes slightly smaller at the lowest Matsubara frequencies in D $\Gamma$ A. In stark contrast to the particle-hole symmetric systems studied above, the momentum dependence is rather small and visible mainly in the real part. This results in a slight deformation of the Fermi surface, which we can see in the left panels of Fig. 11. While purely local correlations cannot change the shape of the Fermi surface with respect to the tight-binding model, nonlocal correlations of D $\Gamma$ A in this

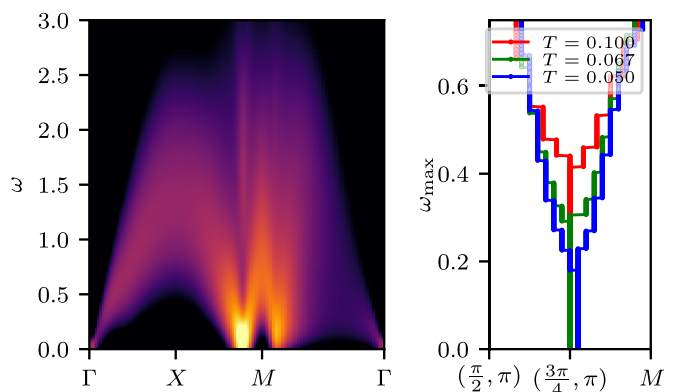


FIG. 10. Left panel: logarithmic plot of the dynamic magnetic structure factor  $\text{Im}\chi_m(\mathbf{q}, \omega)/(1 - e^{-\omega/T})$  at  $U = 8$ ,  $n = 0.85$ , and  $T = 0.05$ , obtained by analytic continuation. The analytic continuation was done with the maximum entropy method [74,75]. Right panel:  $Y$ -shaped spin-excitation dispersion obtained from the dynamic magnetic susceptibility at  $\mathbf{q} = (q_x, \pi)$  for different temperatures  $T$ .

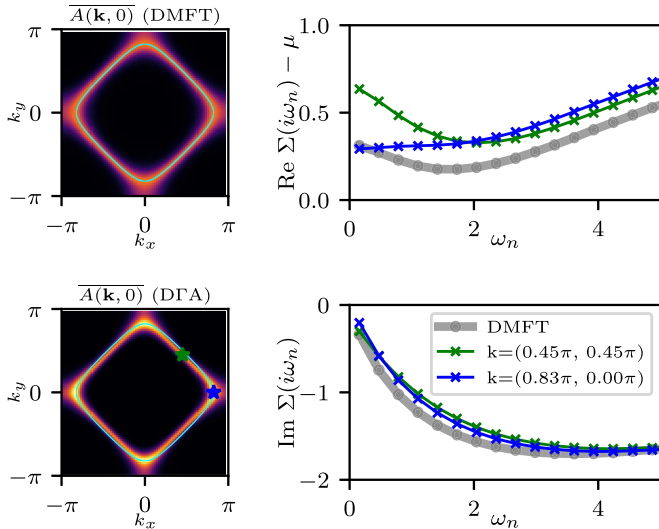


FIG. 11. Fermi surface (FS) and the corresponding real and imaginary part of self-energy as a function of Matsubara frequency as obtained in DMFT and sc-D $\Gamma$ A. For sc-D $\Gamma$ A we show two different momenta on the FS, as indicated with green and blue stars on the FS plot. The FS was obtained by plotting  $\overline{A}_{\mathbf{k}}(0) \approx G(\mathbf{k}, \tau = 1/(2T))$  (which avoids the analytical continuation and averages the spectral function over an interval  $\sim T$  around the FS). The noninteracting tight-binding FS is plotted with a thin cyan line in both FS plots. The parameters are  $T = 0.05$ ,  $U = 8$ ,  $n = 0.85$ .

case make the Fermi surface slightly more “quadratic,” since in the nodal direction the real part of the self-energy at low frequencies is larger than DMFT. Furthermore, we observe that spectral weight is redistributed and more concentrated at the corners.

Our results demonstrate that sc-D $\Gamma$ A works very well also in the doped case. This has been a weak spot for 1-D $\Gamma$ A since in contrast to the symmetric half-filled model, nonlocal correlations change the filling. If the Coulomb interaction is rather large and we are close to half filling, this effect is rather weak. Indeed previous 1-D $\Gamma$ A calculations have hence focused on this parameter regime. However, in other cases the filling of the DMFT serving as an input to the one-shot calculation can and will be quite different from the filling of the 1-D $\Gamma$ A. This renders a self-consistent treatment with an adjustment of the chemical potential obvious, so that the filling remains as that for which the vertex  $\Gamma$  was calculated.

## V. MULTIORBITAL CALCULATIONS

### A. Two-orbital model

In order to demonstrate that self-consistent D $\Gamma$ A also works for more than one orbital, we consider next a simple two-orbital model on a square lattice. Here, electrons can hop only to neighboring atoms with hopping amplitudes  $t_1 = 1$  and  $t_2 = 0.25$  for the two orbitals. This gives rise to a wide and a narrow cosine band with bandwidth 8 and 2, respectively. Along a high-symmetry path, the band structure is shown in Fig. 12 (left) and the Fermi surface of the noninteracting tight-binding model in Fig. 12 (right). This tight-binding model is supplemented by a Coulomb repulsion parametrized in the

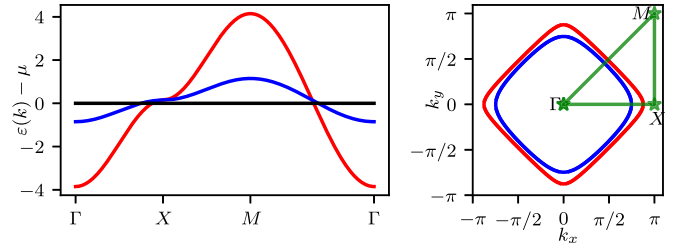


FIG. 12. Two-band model: band structure (left) and Fermi surfaces at  $T = 0.1$  (right). The filling is  $n = 1.7$ , such that the chemical potential is slightly temperature dependent.

Kanamori form with intraorbital interaction  $U = 4$ , Hund’s coupling  $J = 1$ , and interorbital interaction  $V = U - 2J$ . The spin flip and pair hopping processes are of the same magnitude  $J$ . Considering the different bandwidths, the wide band will be weakly correlated, since  $U$  is only one half of the bandwidth. The narrow band, however, is strongly correlated since  $U$  is twice as large as its bandwidth.

In the context of an orbital-selective Mott transition [92–107], such simple half-filled two-band models with different bandwidths and intraorbital hopping have been studied very intensively in DMFT. Early calculations, however, did not include the spin flip and pair hopping processes, but only the density-density interactions for technical reasons. In this situation, the tendency toward an orbital selective Mott transition is largely exaggerated: A spin  $S_z = \pm 1$  formed by the

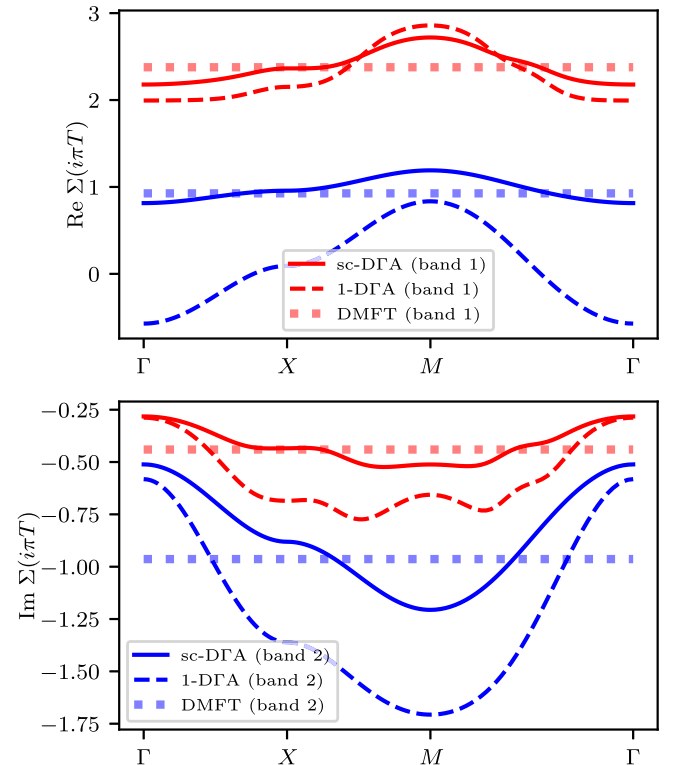


FIG. 13. Real (top) and imaginary part (bottom) of the self energy at the lowest Matsubara frequency for the two band Hubbard model at  $T = 0.1$  along a high-symmetry path through the Brillouin zone.

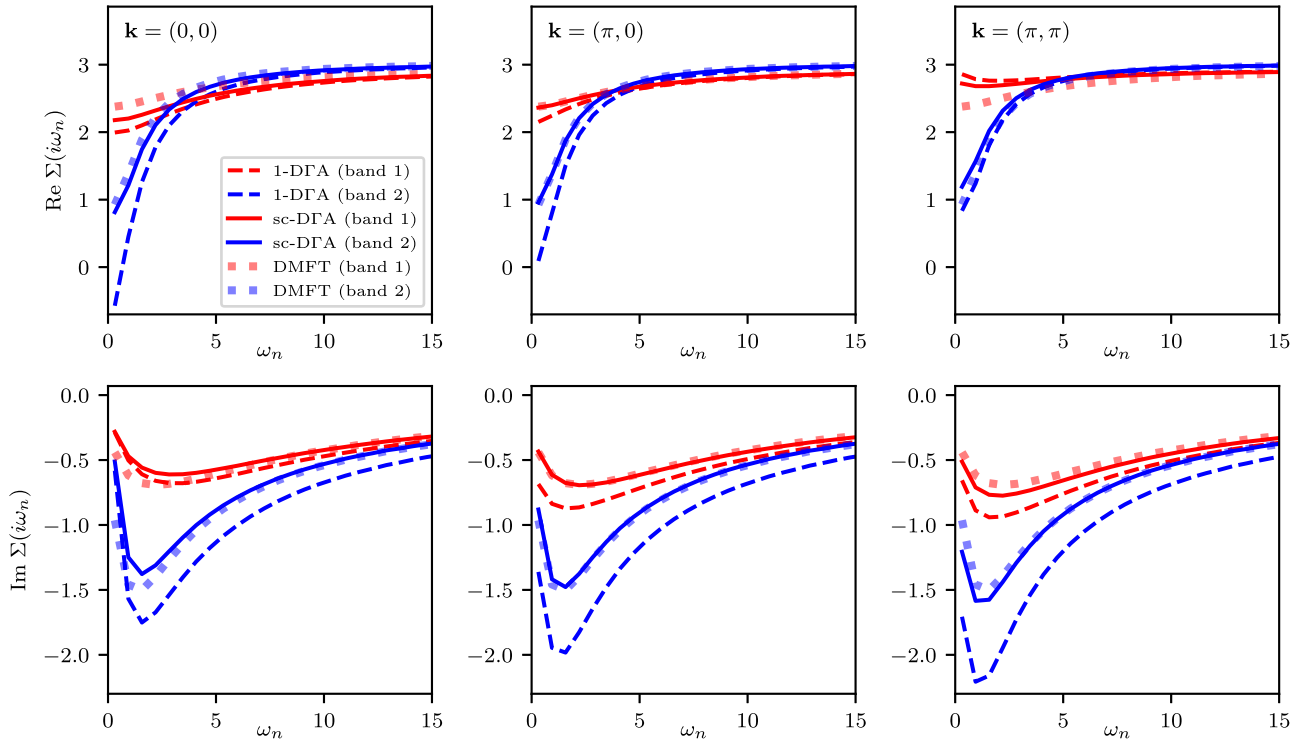


FIG. 14. Real (top) and imaginary (bottom) part of the self-energy vs Matsubara frequency at  $T = 0.1$  for the  $\Gamma$ ,  $X$ , and  $M$  point, comparing DMFT, 1-D $\Gamma$ A, and sc-D $\Gamma$ A for a two-band Hubbard model. The different colors refer to the two bands, as plotted in Fig. 12; the different line types to the different methods.

Hund's exchange cannot undergo a joint SU(4) Kondo effect, while the spin-1 of the SU(2)-symmetric interaction can. As we are primarily interested in testing the sc-D $\Gamma$ A method, we consider here the case where the model is doped away from half filling or  $n = 2$  electrons per site. Specifically, we consider the doping  $n = 1.7$ . This gives rise also to a nonzero real part of the self-energy and (slightly) different fillings of the two orbitals, and hence tests various aspects at the same time.

In Fig. 14 we show the self-energy at selective  $\mathbf{k}$  points. For the given parameters, the 1-D $\Gamma$ A corrections to the self-energy are extremely strong, even exceeding the value of the DMFT self-energy. The reason for this is that we are quite close to an (incommensurate) antiferromagnetic phase transition in DMFT. Immediately before the phase transition, the 1-D $\Gamma$ A corrections become even larger and turn the system insulating.

Similar as for the one-band model, the self-consistency suppresses the antiferromagnetic fluctuations; the actual phase transition occurs only at zero temperature because we are in two dimensions. Hence the sc-D $\Gamma$ A corrections are much weaker at the fixed temperature close to the DMFT phase transition. They will, as a matter of course, become stronger at lower temperatures which are not reachable by 1-D $\Gamma$ A exactly because of the DMFT phase transition. Indeed, Fig. 14 suggests that sc-D $\Gamma$ A is not too distinct from the DMFT result. That is, the self-consistency dampens away much of the one-shot corrections.

However, there is actually a quite important difference: Depending on the  $\mathbf{k}$  point the sc-D $\Gamma$ A imaginary part of the self-energy at low Matsubara frequencies is above or below

the DMFT self-energy in Fig. 14. This becomes even more obvious in Fig. 13, where we plot the self-energy at the lowest Matsubara frequency and see that the low frequency self-energy strongly depends on the momentum. A strong momentum differentiation of the imaginary part of the self-energy (i.e., the scattering rate) has also been reported for a SrVO<sub>3</sub> monolayer [108].

In contrast to the imaginary part, the real part of the self-energy only shows a weak momentum dependence around the DMFT value in Fig. 13. This is different for 1-D $\Gamma$ A where the strong corrections are also reflected in a sizable momentum dependence of the real part of the self-energy; the strongly correlated band (band 2, blue) also displays a sizable overall shift compared to the DMFT result in 1-D $\Gamma$ A.

But let us turn back to the momentum dependence of the self-energy in sc-D $\Gamma$ A. It has a larger influence on the spectral function (Fig. 15) than what one might expect from the Matsubara-frequency dependence in Fig. 14. In Fig. 15 we see, for all three methods, that the weakly correlated band 1 is still close to the tight-binding starting point in Fig. 12, whereas the strongly correlated band 2 is split into an upper Hubbard band (around  $\omega \sim 4$ ), a lower Hubbard band (around  $\omega = -0.5$ ), and a central quasiparticle peak around the Fermi level ( $\omega = 0$ ). The last is better visible in the zoom-in provided by Fig. 16. The aforementioned momentum differentiation of the self-energy results in a considerably wider central quasiparticle band in sc-D $\Gamma$ A than in DMFT or 1-D $\Gamma$ A. In 1-D $\Gamma$ A the strong fluctuations around the phase transition also smear out the central band when reducing temperature from  $T = 0.2$  to  $T = 0.1$ ;  $T = 0.05$  is below the DMFT ordering temperature and a one-shot calculation

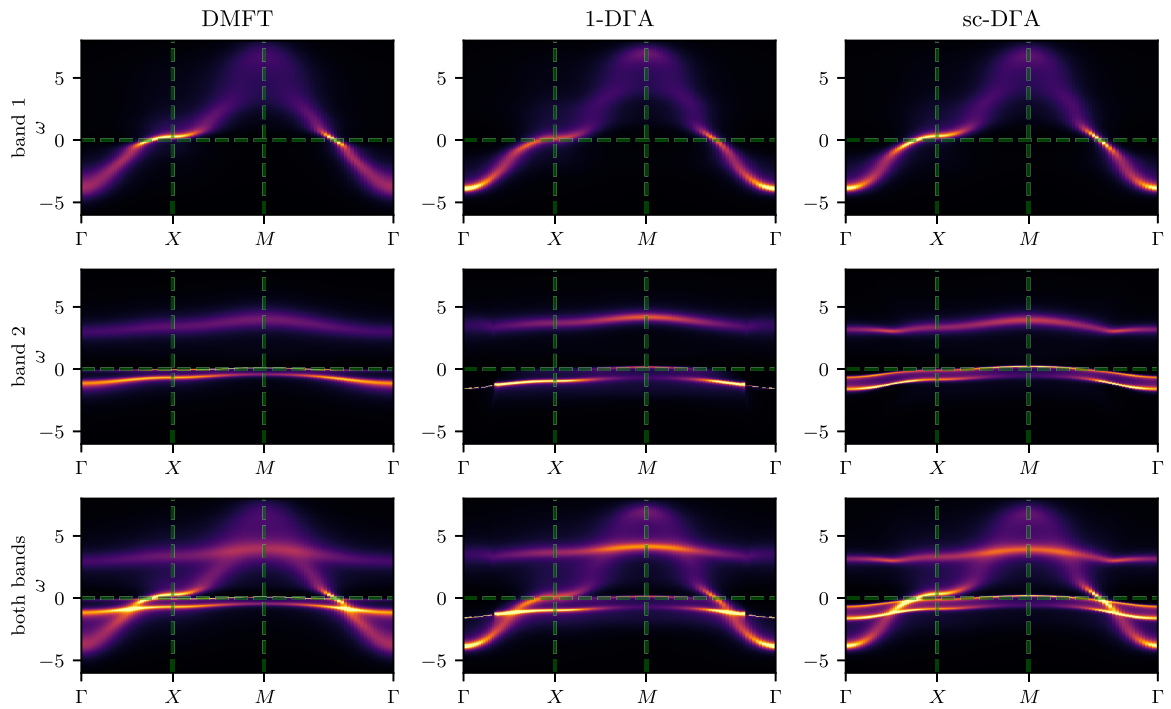


FIG. 15. Momentum-resolved spectral function of the two-orbital Hubbard model at  $T = 0.1$  along a high-symmetry path through the Brillouin zone. The first column shows only the component corresponding to the wide band, the second column only the component corresponding to the narrow band. In the third row the full spectral function is shown.

is hence no longer possible (the reduction of the Néel temperature and susceptibility requires the self-consistency or a Moriya  $\lambda$  correction [19]).

In Fig. 17, we further show the spectral weight at the Fermi level in DMFT and sc-D $\Gamma$ A, summed over both orbitals. Clearly a Fermi surface close to the tight-binding ones

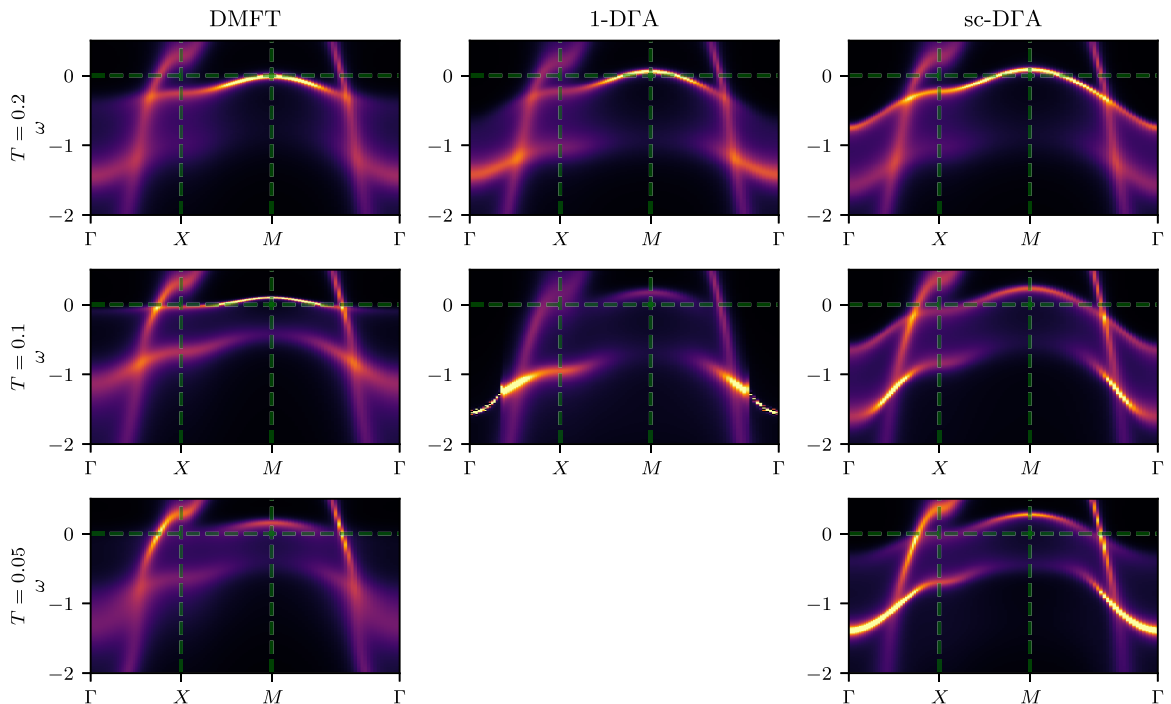


FIG. 16. Low-frequency zoom of momentum-resolved spectral function for the two-orbital Hubbard model at temperatures  $T = 0.2, 0.1, 0.05$  on a path through the Brillouin zone. In the 1-D $\Gamma$ A spectrum at  $T = 0.1$  it is clearly visible that the analytic continuation does not work well in the vicinity of the  $\Gamma$  point. This is a typical issue for 1-D $\Gamma$ A calculations where nonlocal self-energy corrections become large.

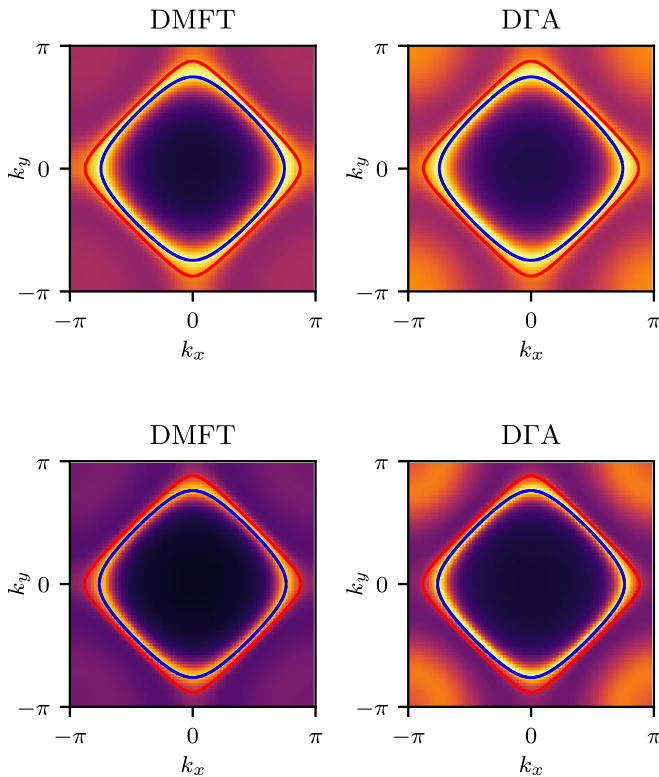


FIG. 17. Spectral weight at the Fermi level  $\overline{A}(\mathbf{k}, 0) \approx G(\mathbf{k}, \tau = 1/2T)$  of the two-band Hubbard model for  $T = 0.1$  (top) and  $T = 0.05$  (bottom), comparing DMFT (left) and sc-D $\Gamma$ A (right) and the tight-binding model without interaction (red and blue lines).

is visible. This stems mostly from the wide, less correlated band. The narrow, strongly correlated band is slightly shifted downwards to lower energy and considerably broadened, cf. Fig. 16. Since the band is so flat, this tiny shift results in a sizable deformation of the spectral weight distribution on the Fermi level: Considering also that  $\overline{A}(\mathbf{k}, 0)$  averages over a frequency range  $\sim T$ , we get diffuse arcs around the  $M$  point, i.e.,  $(\pi, \pi)$ , which is visible in Fig. 17. However, due to the strong renormalization that is already present in DMFT, the narrow band gives only a small contribution to the spectral weight on the Fermi level.

### B. Strontium vanadate

As a second, archetypical multiorbital application we study bulk strontium vanadate  $\text{SrVO}_3$  at room temperature ( $T = 26.3$  meV). This material has served as a testbed for the development of realistic materials calculations with strong correlations and is hence most intensively studied [109–132]. Also the first realistic materials calculations using diagrammatic extensions of DMFT, i.e., *ab initio* D $\Gamma$ A, have been performed for this perovskite [15].  $\text{SrVO}_3$  is a strongly correlated metal with a quasiparticle renormalization of about two [109]. Electronic correlations also lead to a kink in the self-energy and energy-momentum dispersion relation [111, 133–135]. Theoretical calculations and experiments do not indicate any long-range order.

For this realistic *ab initio* calculation, we start with a WIEN2K calculation [136, 137] using the PBE exchange cor-

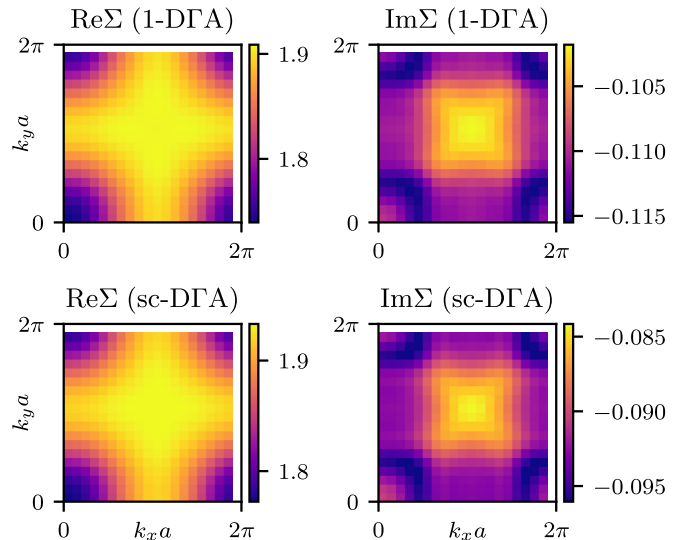


FIG. 18. Momentum dependence of the self-energy of strontium vanadate at the lowest positive Matsubara frequency and  $k_z = 0$ . Upper row: one-shot *ab initio* D $\Gamma$ A, lower row: self-consistent D $\Gamma$ A. The DMFT value is  $(1.861 - 0.104i)$  eV.

relation potential in the generalized gradient approximation (GGA) [138] and a lattice constant of  $a = 3.8$  Å. The calculated band structure is projected onto maximally localized  $t_{2g}$  Wannier orbitals [139–141] using wien2wannier [142]. This three-band Wannier Hamiltonian, available open source [143], is supplemented by a Kanamori Coulomb interaction including the same terms as for the two-band model and parameterized by  $U' = 3.5$  eV,  $J = 0.75$  eV and corresponding  $U = U' + 2J = 5$  eV. The interactions  $U'$  and  $J$  have been calculated by the constrained local density approximation (cLDA) in [109];  $J$  was later slightly corrected as outlined in Sec. 4.1.3 of Ref. [12] to account for the precise way  $J$  enters in Hamiltonian (1) and the cLDA. The difference to earlier *ab initio* D $\Gamma$ A [15–17] calculations, which have been one-shot non-self-consistent calculations, is that we now perform a self-consistent calculation.

As already mentioned, a Moriya- $\lambda$  correction is extremely difficult for such realistic multiorbital calculations. There is not only a magnetic and charge  $\lambda$  for every orbital but additionally also various orbital combinations. Hence, we hold that a self-consistent calculation shall be preferable compared to a high-dimensional fit of the various  $\lambda$  parameters. Also conceptionally it is a clearer approach.

In Fig. 18 we compare the self-energy of the one-shot and self-consistent D $\Gamma$ A calculation. In contrast to the two-band Hubbard model study above, the differences are here only minor. The reason for this is that in the case of the two-band Hubbard model we were close to the DMFT phase transition, whereas  $\text{SrVO}_3$  is rather far away from any phase transition. Hence, the 1-D $\Gamma$ A corrections are much smaller to start with. In such a situation, the self-consistency is not necessary. This justifies *a posteriori* the use of non-self-consistent D $\Gamma$ A in Refs. [15–17].

Nevertheless, Fig. 19 indicates some minor differences between the DMFT, 1-D $\Gamma$ A, and sc-D $\Gamma$ A spectral functions. There are minor differences between 1-D $\Gamma$ A and sc-D $\Gamma$ A

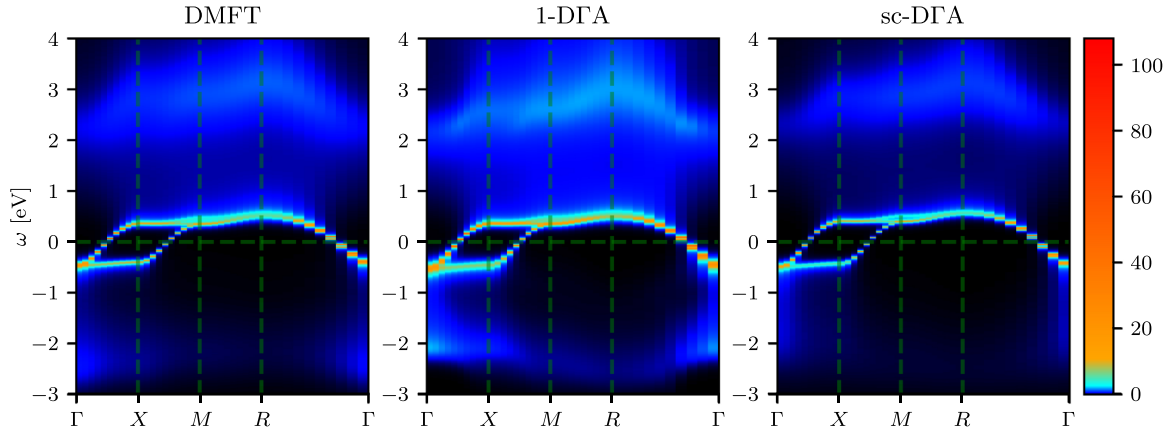


FIG. 19. Momentum-dependent spectral function of SrVO<sub>3</sub>, comparing DMFT, one-shot DΓA, and self-consistent DΓA.

regarding the weight of the lower Hubbard band and the broadening of the quasiparticle peak. This behavior is perfectly in line with the effect of 1-DΓA in other systems studied above. Furthermore there is a shift of the position of the lower Hubbard band toward lower binding energies visible at the  $\Gamma$  point. Experimentally, the maximum of the lower Hubbard band is slightly above  $-2$  eV [109].

## VI. CONCLUSION

We have presented a self-consistent solution of the ladder DΓA equations where the calculated DΓA self-energy is fed back into the Bethe-Salpeter ladder. This dampens the Green's function and thus the overall strength of the ladder, largely reducing the critical temperatures of DMFT. Hitherto, a similar effect has been achieved by a Moriyaesque  $\lambda$  correction for one-band models; multiorbital models have only been studied by one-shot, non-self-consistent, and non- $\lambda$ -corrected calculations. Applying such a  $\lambda$  correction to multiorbital or doped systems is difficult, to say the least. One-shot calculations, on the other hand, are disputable whenever the nonlocal corrections to DMFT become large. Our paper demonstrates that conceptionally clean self-consistent calculations are indeed feasible and work well, also for multiorbital and doped systems.

For the one-band Hubbard model we have benchmarked the method against previous ( $\lambda$ -corrected and parquet) DΓA and numerically exact DiagMC results at weak coupling. We find an excellent agreement up to the point where the susceptibilities become huge, where self-consistent DΓA yields a somewhat reduced susceptibility. The self-consistency allows applying DΓA even in the close vicinity of the divergence lines of the vertex, at strong coupling and for doped systems.

For the two-band Hubbard model we study the regime close to the DMFT phase transition. Here, the one-shot DΓA corrections are large but the self-consistency mitigates this to a large extent. While the frequency dependence eventually looks similar to that of DMFT, there is a sizable momentum dependence which leads to a widening of the quasiparticle band. In the case of SrVO<sub>3</sub> we have performed realistic *ab initio* DΓA materials calculations. Here, we are not close to any phase transition and the difference between one-shot and self-consistent *ab initio* DΓA is minute.

## ACKNOWLEDGMENTS

We thank Thomas Schäfer, Fedor Šimkovic, and Patrick Chalupa for providing reference data and Patrik Thunström, Anna Galler, and Jan M. Tomczak for fruitful discussions and valuable advice. J.K. further thanks Oleg Janson, Alexander Lichtenstein, Andrey Katanin, Jan Kuneš, Evgeny Stepanov, Patrik Gunacker, Tin Ribic, Dominique Geffroy, and Benedikt Hartl for fruitful discussions. This work has been supported financially by the European Research Council under the European Union's Seventh Framework Program (FP/2007-2013)/ERC Grant Agreement No. 306447 and by the Austrian Science Fund (FWF) through Projects No. P 30997, No. P 30819, and No. P 32044. Calculations have been done in part on the Vienna Scientific Cluster (VSC).

## APPENDIX A: IMPLEMENTATION

For the practical evaluation of the DΓA equations (21)–(23), we use the *ab initio* DΓA code [17]. Here we describe the details of the implementation, which are closely connected to *ab initio* DΓA. Solving the aforementioned equations self-consistently means that the *ab initio* DΓA code is executed several times in a loop in order to do a fixed-point iteration. Before each iteration, we create an updated trial input, until the point where the output does not differ from the input anymore. Therefore, in order to describe the details of the updates, we have to recapitulate the input structure of *ab initio* DΓA first.

Apart from the system-defining parameters (tight-binding Hamiltonian and  $U$  matrix) the following quantities are required as input:

- (1) lattice self-energy  $\Sigma^k$  (can also be momentum independent)
- (2) impurity self-energy  $\Sigma_{\text{imp}}^v$  (can be identical to the lattice self-energy, as in 1-DΓA)
- (3) impurity Green's function  $g^v$
- (4) impurity two-particle Green's function  $G^{vv'\omega}$

The update proceeds in the two steps described in the following.

### 1. Update of the self-energy and one-particle Green's function

This step defines the update. We take trial and result self-energies from several preceding iterations and compose a new

trial self-energy  $\Sigma_{\text{trial}}^{k(j)}$  for the  $j$ th iteration. This prediction is usually made by the Anderson acceleration algorithm [67,68] (also known as Pulay mixing [144] or direct inversion in iterative subspace, DIIS [145]). This trial self-energy is then used to compute a new local propagator  $G_{\text{loc}}^{v(j)}$  by

$$G_{\text{loc}}^{v(j)} = \frac{1}{V_{\text{BZ}}} \int d^d k [(iv + \mu^{(j)})\mathbb{1} - h(\mathbf{k}) - \Sigma_{\text{trial}}^{k(j)}]^{-1}, \quad (\text{A1})$$

where the chemical potential  $\mu^{(j)}$  is adapted such that the expectation value of the particle number stays at the desired value. The change of the chemical potential usually stays in the range of a few percent. Once the new local Green's function is determined, we project (downfold) it to the correlated impurity subspaces. Thus, each impurity  $I$  obtains its new Green's function  $g_I^{v(j)}$ .

## 2. Update of impurity quantities

This step is inherent to our specific implementation of *ab initio* DΓA and not part of the algorithm *per se*. But since *ab initio* DΓA reads the one- and two-particle Green's function instead of the irreducible vertex, we need to “wrap” the irreducible vertex (unchanged throughout all iterations) in the new impurity propagator by means of the Bethe-Salpeter equation. In order to avoid direct computation of the irreducible vertex, we compute the updated generalized susceptibility for iteration ( $j$ ) in channel  $r$  by

$$\chi_r^{(j)} = \chi_r^{\text{DMFT}} [\chi_r^{\text{DMFT}} + \chi_0^{(j)} - \chi_0^{(j)} (\chi_0^{\text{DMFT}})^{-1} \chi_r^{\text{DMFT}}]^{-1} \chi_0^{(j)}. \quad (\text{A2})$$

Note that all susceptibilities in this equation are compound-index matrices in the orbital space of the impurity and fermionic frequencies. The new impurity one-particle Green's function enters into this equation only through  $\chi_0^{(j)}$  of Eq. (9), where updated impurity Green's functions  $g^{(j)}$  are used. The two-particle Green's function is obtained by dividing through  $\beta$  and adding a disconnected part, according to Eq. (7).

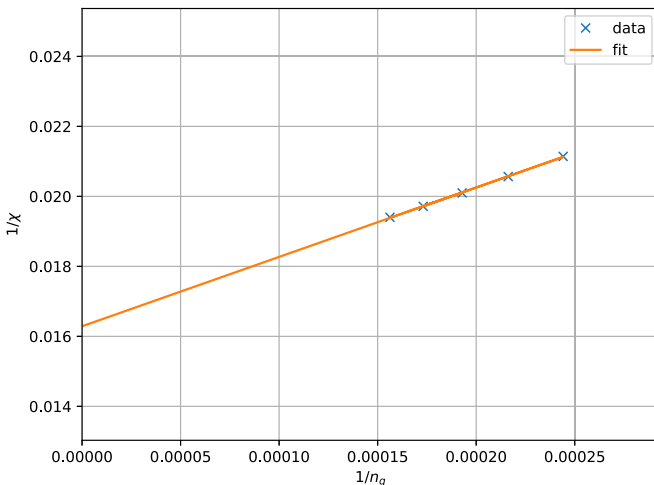


FIG. 20. Extrapolation of antiferromagnetic susceptibility of the square-lattice Hubbard model with  $U = 2$  at  $T = 0.05$ . The largest  $\mathbf{q}$  grid is  $80 \times 80$ .

Furthermore, it is necessary to compute an updated (“fake”) impurity self-energy by the equation of motion. The reason for this can be seen in Eq. (75) of Ref. [15]. There, the DMFT self-energy appears as a separate term. However, in its essence it is not the DMFT self-energy but rather the result of the Schwinger-Dyson equation of motion for the impurity [146]. In Ref. [15], this term is subtracted and substituted by the actual DMFT self-energy, in order to mitigate effects of finite frequency boxes. Therefore, we compute the impurity self-energy from the equation of motion,

$$\Sigma_{\text{con},m,I}^{v(j)} = \frac{1}{\beta} \sum_{v'\omega} \sum_{lhn} U_{l,m} G_{\text{con},l,nlhm}^{v'\omega(j)} / g_{l,m}^{v(j)}, \quad (\text{A3})$$

using both the new ( $j$ ) and the DMFT one- and two-particle Green's function. The index  $I$  labels the  $I$ th impurity of the unit cell. Importantly, the frequency boxes have to be identical. Then the difference of these two self-energies is added to the DMFT self-energy and taken as the new (fake) impurity self-energy. In this way the effects of finite-box summation are canceled. We emphasize that the “fake” impurity self-energy is merely an auxiliary quantity and never used to extract any physical properties of the result. Only the lattice self-energy is subject to physical interpretation in our computations.

## APPENDIX B: EXTRAPOLATION OF THE SUSCEPTIBILITY

Since we are quite limited in the number of  $\mathbf{q}$  points that we can use in our calculation, we have to do an extrapolation of the magnetic susceptibility. This is possible due to the observation that the inverse of the antiferromagnetic susceptibility depends linearly on the inverse of the number of  $\mathbf{q}$  points. In particular, the extrapolation was necessary for sc-DΓA on the square-lattice Hubbard model with  $U = 2$  at  $T = 0.05$  and  $T = 0.04$ . There the DΓA calculation was done with  $48 \times 48$ ,  $64 \times 64$ ,  $68 \times 68$ ,  $72 \times 72$ ,  $76 \times 76$ ,  $80 \times 80$   $\mathbf{k}$  and  $\mathbf{q}$  points. In Fig. 20 and Fig. 21 it is visible that the extrapolation with the above-mentioned linear relation is indeed possible. Although a deviation from this behavior is to

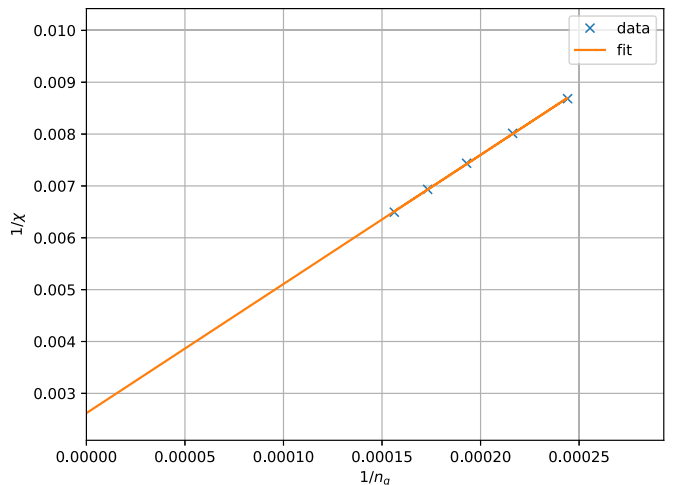


FIG. 21. Extrapolation of antiferromagnetic susceptibility of the square-lattice Hubbard model with  $U = 2$  at  $T = 0.04$ . The largest  $\mathbf{q}$  grid is  $80 \times 80$ .



be expected as  $n_{\mathbf{q}} \rightarrow \infty$ , it can only lead to a small change in the logarithmic plot in Fig. 4 and thus our conclusions remain unchanged. On the other hand, for  $\mathbf{k}$  and  $\mathbf{q}$  grids of  $48 \times 48$  or

larger, we find that the self-energy is practically independent on the number of  $\mathbf{k}$  and  $\mathbf{q}$  points, such that no extrapolation is necessary there.

- 
- [1] P. Hohenberg and W. Kohn, *Phys. Rev.* **136**, B864 (1964).
- [2] R. O. Jones and O. Gunnarsson, *Rev. Mod. Phys.* **61**, 689 (1989).
- [3] W. Metzner and D. Vollhardt, *Phys. Rev. Lett.* **62**, 324 (1989).
- [4] A. Georges and G. Kotliar, *Phys. Rev. B* **45**, 6479 (1992).
- [5] M. Jarrell, *Phys. Rev. Lett.* **69**, 168 (1992).
- [6] A. Georges, G. Kotliar, W. Krauth, and M. J. Rozenberg, *Rev. Mod. Phys.* **68**, 13 (1996).
- [7] G. Kotliar and D. Vollhardt, *Phys. Today* **57**(3), 53 (2004).
- [8] V. I. Anisimov, A. I. Poteryaev, M. A. Korotin, A. O. Anokhin, and G. Kotliar, *J. Phys.: Condens. Matter* **9**, 7359 (1997).
- [9] A. I. Lichtenstein and M. I. Katsnelson, *Phys. Rev. B* **57**, 6884 (1998).
- [10] K. Held, I. A. Nekrasov, G. Keller, V. Eyert, N. Blümer, A. K. McMahan, R. T. Scalettar, T. Pruschke, V. I. Anisimov, and D. Vollhardt, *Phys. Status Solidi B* **243**, 2599 (2006).
- [11] G. Kotliar, S. Y. Savrasov, K. Haule, V. S. Oudovenko, O. Parcollet, and C. A. Marianetti, *Rev. Mod. Phys.* **78**, 865 (2006).
- [12] K. Held, *Adv. Phys.* **56**, 829 (2007).
- [13] E. Gull, A. J. Millis, A. I. Lichtenstein, A. N. Rubtsov, M. Troyer, and P. Werner, *Rev. Mod. Phys.* **83**, 349 (2011).
- [14] G. Rohringer, H. Hafermann, A. Toschi, A. A. Katanin, A. E. Antipov, M. I. Katsnelson, A. I. Lichtenstein, A. N. Rubtsov, and K. Held, *Rev. Mod. Phys.* **90**, 025003 (2018).
- [15] A. Galler, P. Thunström, P. Gunacker, J. M. Tomczak, and K. Held, *Phys. Rev. B* **95**, 115107 (2017).
- [16] A. Galler, J. Kaufmann, P. Gunacker, M. Pickem, P. Thunström, J. M. Tomczak, and K. Held, *J. Phys. Soc. Jpn.* **87**, 041004 (2018).
- [17] A. Galler, P. Thunström, J. Kaufmann, M. Pickem, J. M. Tomczak, and K. Held, *Comput. Phys. Commun.* **245**, 106847 (2019).
- [18] A. Toschi, A. A. Katanin, and K. Held, *Phys. Rev. B* **75**, 045118 (2007).
- [19] A. A. Katanin, A. Toschi, and K. Held, *Phys. Rev. B* **80**, 075104 (2009).
- [20] G. Rohringer and A. Toschi, *Phys. Rev. B* **94**, 125144 (2016).
- [21] G. Rohringer, A. Toschi, A. Katanin, and K. Held, *Phys. Rev. Lett.* **107**, 256402 (2011).
- [22] T. Schäfer, A. A. Katanin, K. Held, and A. Toschi, *Phys. Rev. Lett.* **119**, 046402 (2017).
- [23] T. Schäfer, A. A. Katanin, M. Kitatani, A. Toschi, and K. Held, *Phys. Rev. Lett.* **122**, 227201 (2019).
- [24] M. Kitatani, T. Schäfer, H. Aoki, and K. Held, *Phys. Rev. B* **99**, 041115(R) (2019).
- [25] M. Kitatani, L. Si, O. Janson, R. Arita, Z. Zhong, and K. Held, *npj Quantum Mater.* **5**, 59 (2020).
- [26] A. N. Rubtsov, M. I. Katsnelson, and A. I. Lichtenstein, *Phys. Rev. B* **77**, 033101 (2008).
- [27] H. Hafermann, G. Li, A. N. Rubtsov, M. I. Katsnelson, A. I. Lichtenstein, and H. Monien, *Phys. Rev. Lett.* **102**, 206401 (2009).
- [28] D. Hirschmeier, H. Hafermann, E. Gull, A. I. Lichtenstein, and A. E. Antipov, *Phys. Rev. B* **92**, 144409 (2015).
- [29] A. E. Antipov, E. Gull, and S. Kirchner, *Phys. Rev. Lett.* **112**, 226401 (2014).
- [30] T. Ribic, P. Gunacker, and K. Held, *Phys. Rev. B* **98**, 125106 (2018).
- [31] E. G. C. P. van Loon, M. I. Katsnelson, and H. Hafermann, *Phys. Rev. B* **98**, 155117 (2018).
- [32] A. Tanaka, *Phys. Rev. B* **99**, 205133 (2019).
- [33] A. Valli, T. Schäfer, P. Thunström, G. Rohringer, S. Andergassen, G. Sangiovanni, K. Held, and A. Toschi, *Phys. Rev. B* **91**, 115115 (2015).
- [34] G. Li, N. Wentzell, P. Pudleiner, P. Thunström, and K. Held, *Phys. Rev. B* **93**, 165103 (2016).
- [35] G. Li, A. Kauch, P. Pudleiner, and K. Held, *Comput. Phys. Commun.* **241**, 146 (2019).
- [36] A. Kauch, F. Hörbinger, G. Li, and K. Held, *arXiv:1901.09743*.
- [37] C. J. Eckhardt, C. Honerkamp, K. Held, and A. Kauch, *Phys. Rev. B* **101**, 155104 (2020).
- [38] For the parquet dual fermion approach, see Refs. [147–149].
- [39] C. De Dominicis and P. C. Martin, *J. Math. Phys.* **5**, 14 (1964).
- [40] C. De Dominicis and P. C. Martin, *J. Math. Phys.* **5**, 31 (1964).
- [41] N. E. Bickers, in *Theoretical Methods for Strongly Correlated Electrons. CRM Series in Mathematical Physics*, edited by D. Sénéchal, A.-M. Tremblay, and C. Bourbonnais (Springer, New York, 2004).
- [42] A. N. Vasil'ev, *Functional Methods in Quantum Field Theory and Statistical Physics*, 1st ed., Vol. 1 (Taylor and Francis Group, London, 1998).
- [43] A. Kauch, P. Pudleiner, K. Astleithner, P. Thunström, T. Ribic, and K. Held, *Phys. Rev. Lett.* **124**, 047401 (2020).
- [44] G. Rohringer, A. Valli, and A. Toschi, *Phys. Rev. B* **86**, 125114 (2012).
- [45] P. Gunacker, M. Wallerberger, E. Gull, A. Hausoel, G. Sangiovanni, and K. Held, *Phys. Rev. B* **92**, 155102 (2015).
- [46] M. Wallerberger, A. Hausoel, P. Gunacker, A. Kowalski, N. Parragh, F. Goth, K. Held, and G. Sangiovanni, *Comput. Phys. Commun.* **235**, 388 (2019).
- [47] And often dangerous.
- [48] T. Schäfer, A. Toschi, and K. Held, *J. Magn. Magn. Mater.* **400**, 107 (2016), proceedings of the 20th International Conference on Magnetism (Barcelona) 5–10 July 2015.
- [49] F. B. Kugler and J. von Delft, *New J. Phys.* **20**, 123029 (2018).
- [50] C. Hille, F. B. Kugler, C. J. Eckhardt, Y.-Y. He, A. Kauch, C. Honerkamp, A. Toschi, and S. Andergassen, *Phys. Rev. Research* **2**, 033372 (2020).
- [51] W. Metzner, M. Salmhofer, C. Honerkamp, V. Meden, and K. Schönhammer, *Rev. Mod. Phys.* **84**, 299 (2012).
- [52] That is, cutting any two Green's function lines does not separate the Feynman diagram into two pieces.
- [53] It is not necessary to take  $\Lambda$  from DMFT. One could improve the auxiliary Anderson impurity model, so that it produced the

- same local Green's function as the one resulting from p-DΓA. It would add another level of self-consistency. This impurity update turned out to be unnecessary for the parameters presented in this paper.
- [54] C. Husemann and M. Salmhofer, *Phys. Rev. B* **79**, 195125 (2009).
- [55] C. J. Eckhardt, G. A. H. Schober, J. Ehrlich, and C. Honerkamp, *Phys. Rev. B* **98**, 075143 (2018).
- [56] T. Schäfer, G. Rohringer, O. Gunnarsson, S. Ciuchi, G. Sangiovanni, and A. Toschi, *Phys. Rev. Lett.* **110**, 246405 (2013).
- [57] T. Schäfer, S. Ciuchi, M. Wallerberger, P. Thunström, O. Gunnarsson, G. Sangiovanni, G. Rohringer, and A. Toschi, *Phys. Rev. B* **94**, 235108 (2016).
- [58] O. Gunnarsson, G. Rohringer, T. Schäfer, G. Sangiovanni, and A. Toschi, *Phys. Rev. Lett.* **119**, 056402 (2017).
- [59] J. Vučićević, N. Wentzell, M. Ferrero, and O. Parcollet, *Phys. Rev. B* **97**, 125141 (2018).
- [60] P. Chalupa, P. Gunacker, T. Schäfer, K. Held, and A. Toschi, *Phys. Rev. B* **97**, 245136 (2018).
- [61] In some cases it may be preferable to take the nonlocal particle-particle fluctuations as dominant and approximate the particle-hole channel to the local level. In the scope of this paper we treat however only problems with dominant fluctuations in the particle-hole channel.
- [62] N. D. Mermin and H. Wagner, *Phys. Rev. Lett.* **17**, 1307 (1966).
- [63] T. Schäfer, N. Wentzell, F. Šimkovic IV, Y.-Y. He, C. Hille, M. Klett, C. J. Eckhardt, B. Arzhang, V. Harkov, F.-M. L. Régent, A. Kirsch, Y. Wang, A. J. Kim, E. Kozik, E. A. Stepanov, A. Kauch, S. Andergassen, P. Hansmann, D. Rohe, Y. M. Vilk, J. P. F. LeBlanc, S. Zhang, A. M. S. Tremblay, M. Ferrero, O. Parcollet, and A. Georges, *Phys. Rev. X* [to be published (2021)], [arXiv:2006.10769](https://arxiv.org/abs/2006.10769).
- [64] H. Miyahara, R. Arita, and H. Ikeda, *Phys. Rev. B* **87**, 045113 (2013).
- [65] S. Arya, P. V. Sriluckshmy, S. R. Hassan, and A.-M. S. Tremblay, *Phys. Rev. B* **92**, 045111 (2015).
- [66] A. M. S. Tremblay, in *Strongly Correlated Systems: Theoretical Methods*, edited by F. Mancini and A. Avella (Springer, Berlin, Heidelberg, 2011), Chap. 13, p. 409–455.
- [67] D. G. Anderson, *J. ACM* **12**, 547 (1965).
- [68] H. F. Walker and P. Ni, *SIAM J. Numer. Anal.* **49**, 1715 (2011).
- [69] T. Ayril and O. Parcollet, *Phys. Rev. B* **94**, 075159 (2016).
- [70] Actually, for Kanamori interaction we find  $M_{\text{comp}}(M) = 6x_N$  where  $x_N = 3M^2 - 2M$  are *octagonal numbers*.
- [71] J. Kaufmann, P. Gunacker, A. Kowalski, G. Sangiovanni, and K. Held, *Phys. Rev. B* **100**, 075119 (2019).
- [72] P. Kappl, M. Wallerberger, J. Kaufmann, M. Pickem, and K. Held, *Phys. Rev. B* **102**, 085124 (2020).
- [73] J. Kuneš, *Phys. Rev. B* **83**, 085102 (2011).
- [74] D. Geffroy, J. Kaufmann, A. Hariki, P. Gunacker, A. Hausoel, and J. Kuneš, *Phys. Rev. Lett.* **122**, 127601 (2019).
- [75] J. Kaufmann, *ana\_cont*: Package for analytic continuation of many-body green's functions, [https://github.com/josefkaufmann/ana\\_cont](https://github.com/josefkaufmann/ana_cont) (2020).
- [76] Y.M. Vilk and A.-M.S. Tremblay, *J. Phys. I (France)* **7**, 1309 (1997).
- [77] A. N. Rubtsov, M. I. Katsnelson, A. I. Lichtenstein, and A. Georges, *Phys. Rev. B* **79**, 045133 (2009).
- [78] D. Rost, E. V. Gorelik, F. Assaad, and N. Blümer, *Phys. Rev. B* **86**, 155109 (2012).
- [79] T. Schäfer, F. Geles, D. Rost, G. Rohringer, E. Arrigoni, K. Held, N. Blümer, M. Aichhorn, and A. Toschi, *Phys. Rev. B* **91**, 125109 (2015).
- [80] J. González, F. Guinea, and M. A. H. Vozmediano, *Phys. Rev. Lett.* **84**, 4930 (2000).
- [81] C. J. Halboth and W. Metzner, *Phys. Rev. Lett.* **85**, 5162 (2000).
- [82] C. Honerkamp and M. Salmhofer, *Phys. Rev. Lett.* **87**, 187004 (2001).
- [83] W. Wu, M. S. Scheurer, M. Ferrero, and A. Georges, *Phys. Rev. Research* **2**, 033067 (2020).
- [84] F. Šimkovic and E. Kozik, *Phys. Rev. B* **100**, 121102(R) (2019).
- [85] In this case the Ward identity relating the irreducible vertex and self-energy  $\Gamma = \frac{\delta\Sigma}{\delta G}$  is violated. This is also the case in the parquet approach, but certainly to a much smaller extent.
- [86] E. Gull, O. Parcollet, and A. J. Millis, *Phys. Rev. Lett.* **110**, 216405 (2013).
- [87] K.-S. Chen, Z. Y. Meng, S.-X. Yang, T. Pruschke, J. Moreno, and M. Jarrell, *Phys. Rev. B* **88**, 245110 (2013).
- [88] J. Otsuki, H. Hafermann, and A. I. Lichtenstein, *Phys. Rev. B* **90**, 235132 (2014).
- [89] C. J. Jia, E. A. Nowadnick, K. Wohlfeld, Y. F. Kung, C.-C. Chen, S. Johnston, T. Tohyama, B. Moritz, and T. P. Devereaux, *Nat. Commun.* **5**, 3314 (2014).
- [90] J. P. F. LeBlanc, S. Li, X. Chen, R. Levy, A. E. Antipov, A. J. Millis, and E. Gull, *Phys. Rev. B* **100**, 075123 (2019).
- [91] M. K. Chan, C. J. Dorow, L. Mangin-Thro, Y. Tang, Y. Ge, M. J. Veit, G. Yu, X. Zhao, A. D. Christianson, J. T. Park, Y. Sidis, P. Steffens, D. L. Abernathy, P. Bourges, and M. Greven, *Nat. Commun.* **7**, 10819 (2016).
- [92] V. Anisimov, I. Nekrasov, D. Kondakov, T. Rice, and M. Sigrist, *Eur. Phys. J. B* **25**, 191 (2002).
- [93] A. Liebsch, *Europhys. Lett.* **63**, 97 (2003).
- [94] A. Liebsch, *Phys. Rev. B* **70**, 165103 (2004).
- [95] A. Koga, N. Kawakami, T. M. Rice, and M. Sigrist, *Phys. Rev. B* **72**, 045128 (2005).
- [96] S. Biermann, L. de' Medici, and A. Georges, *Phys. Rev. Lett.* **95**, 206401 (2005).
- [97] R. Arita and K. Held, *Phys. Rev. B* **72**, 201102(R) (2005).
- [98] C. Knecht, N. Blümer, and P. G. J. van Dongen, *Phys. Rev. B* **72**, 081103(R) (2005).
- [99] S. Sakai, R. Arita, K. Held, and H. Aoki, *Phys. Rev. B* **74**, 155102 (2006).
- [100] M. Ferrero, F. Becca, M. Fabrizio, and M. Capone, *Phys. Rev. B* **72**, 205126 (2005).
- [101] T. A. Costi and A. Liebsch, *Phys. Rev. Lett.* **99**, 236404 (2007).
- [102] A. Koga, N. Kawakami, T. M. Rice, and M. Sigrist, *Phys. Rev. Lett.* **92**, 216402 (2004).
- [103] M. Greger, M. Kollar, and D. Vollhardt, *Phys. Rev. Lett.* **110**, 046403 (2013).
- [104] A. Valli, H. Das, G. Sangiovanni, T. Saha-Dasgupta, and K. Held, *Phys. Rev. B* **92**, 115143 (2015).
- [105] L. F. Tocchio, F. Arrigoni, S. Sorella, and F. Becca, *J. Phys.: Condens. Matter* **28**, 105602 (2016).
- [106] M.-T. Philipp, M. Wallerberger, P. Gunacker, and K. Held, *Eur. Phys. J. B* **90**, 114 (2017).

- [107] W. Hu, R. T. Scalettar, E. W. Huang, and B. Moritz, *Phys. Rev. B* **95**, 235122 (2017).
- [108] M. Pickem, J. Kaufmann, J. M. Tomczak, and K. Held, [arXiv:2008.12227](https://arxiv.org/abs/2008.12227).
- [109] A. Sekiyama, H. Fujiwara, S. Imada, S. Suga, H. Eisaki, S. I. Uchida, K. Takegahara, H. Harima, Y. Saitoh, I. A. Nekrasov, G. Keller, D. E. Kondakov, A. V. Kozhevnikov, T. Pruschke, K. Held, D. Vollhardt, and V. I. Anisimov, *Phys. Rev. Lett.* **93**, 156402 (2004).
- [110] E. Pavarini, S. Biermann, A. Poteryaev, A. I. Lichtenstein, A. Georges, and O. K. Andersen, *Phys. Rev. Lett.* **92**, 176403 (2004).
- [111] I. A. Nekrasov, K. Held, G. Keller, D. E. Kondakov, T. Pruschke, M. Kollar, O. K. Andersen, V. I. Anisimov, and D. Vollhardt, *Phys. Rev. B* **73**, 155112 (2006).
- [112] K. Maiti, U. Manju, S. Ray, P. Mahadevan, I. H. Inoue, C. Carbone, and D. D. Sarma, *Phys. Rev. B* **73**, 052508 (2006).
- [113] I. Leonov, V. I. Anisimov, and D. Vollhardt, *Phys. Rev. Lett.* **112**, 146401 (2014).
- [114] M. Karolak, T. O. Wehling, F. Lechermann, and A. I. Lichtenstein, *J. Phys.: Condens. Matter* **23**, 085601 (2011).
- [115] H. Lee, K. Foyevtsova, J. Ferber, M. Aichhorn, H. O. Jeschke, and R. Valenti, *Phys. Rev. B* **85**, 165103 (2012).
- [116] M. Casula, A. Rubtsov, and S. Biermann, *Phys. Rev. B* **85**, 035115 (2012).
- [117] J. M. Tomczak, M. Casula, T. Miyake, F. Aryasetiawan, and S. Biermann, *Europhys. Lett.* **100**, 67001 (2012).
- [118] C. Taranto, M. Kaltak, N. Parragh, G. Sangiovanni, G. Kresse, A. Toschi, and K. Held, *Phys. Rev. B* **88**, 165119 (2013).
- [119] T. Miyake, C. Martins, R. Sakuma, and F. Aryasetiawan, *Phys. Rev. B* **87**, 115110 (2013).
- [120] R. Sakuma, P. Werner, and F. Aryasetiawan, *Phys. Rev. B* **88**, 235110 (2013).
- [121] J. M. Tomczak, M. Casula, T. Miyake, and S. Biermann, *Phys. Rev. B* **90**, 165138 (2014).
- [122] H. Wadati, J. Mravlje, K. Yoshimatsu, H. Kumigashira, M. Oshima, T. Sugiyama, E. Ikenaga, A. Fujimori, A. Georges, A. Radetinac, K. S. Takahashi, M. Kawasaki, and Y. Tokura, *Phys. Rev. B* **90**, 205131 (2014).
- [123] T. Ribic, E. Assmann, A. Tóth, and K. Held, *Phys. Rev. B* **90**, 165105 (2014).
- [124] Z. Zhong, M. Wallerberger, J. M. Tomczak, C. Taranto, N. Parragh, A. Toschi, G. Sangiovanni, and K. Held, *Phys. Rev. Lett.* **114**, 246401 (2015).
- [125] K. Nakamura, Y. Nohara, Y. Yosimoto, and Y. Nomura, *Phys. Rev. B* **93**, 085124 (2016).
- [126] L. Boehnke, F. Nilsson, F. Aryasetiawan, and P. Werner, *Phys. Rev. B* **94**, 201106(R) (2016).
- [127] S. Backes, T. C. Rödel, F. Fortuna, E. Frantzeskakis, P. Le Fèvre, F. Bertran, M. Kobayashi, R. Yukawa, T. Mitsuhashi, M. Kitamura, K. Horiba, H. Kumigashira, R. Saint-Martin, A. Fouchet, B. Berini, Y. Dumont, A. J. Kim, F. Lechermann, H. O. Jeschke, M. J. Rozenberg, R. Valenti, and A. F. Santander-Syro, *Phys. Rev. B* **94**, 241110(R) (2016).
- [128] S. Bhandary, E. Assmann, M. Aichhorn, and K. Held, *Phys. Rev. B* **94**, 155131 (2016).
- [129] J. J. M. Tomczak, P. Liu, A. Toschi, G. Kresse, and K. Held, *Eur. Phys. J.: Spec. Top.* **226**, 2565 (2017).
- [130] J. Kaufmann, P. Gunacker, and K. Held, *Phys. Rev. B* **96**, 035114 (2017).
- [131] D. Bauernfeind, M. Zingl, R. Triebel, M. Aichhorn, and H. G. Evertz, *Phys. Rev. X* **7**, 031013 (2017).
- [132] J.-H. Sim and M. J. Han, *Phys. Rev. B* **100**, 115151 (2019).
- [133] K. Byczuk, M. Kollar, K. Held, Y.-F. Yang, I. A. Nekrasov, Th. Pruschke, and D. Vollhardt, *Nat. Phys.* **3**, 168 (2007).
- [134] S. Aizaki, T. Yoshida, K. Yoshimatsu, M. Takizawa, M. Minohara, S. Ideta, A. Fujimori, K. Gupta, P. Mahadevan, K. Horiba, H. Kumigashira, and M. Oshima, *Phys. Rev. Lett.* **109**, 056401 (2012).
- [135] K. Held, R. Peters, and A. Toschi, *Phys. Rev. Lett.* **110**, 246402 (2013).
- [136] P. Blaha, K. Schwarz, G. K. H. Madsen, D. Kvasnicka, and J. Luitz, *An Augmented Plane Wave + Local Orbitals Program for Calculating Crystal Properties* (Technische Universität Wien, Vienna, 2001).
- [137] K. Schwarz, P. Blaha, and G. Madsen, *Comput. Phys. Commun.* **147**, 71 (2002).
- [138] J. P. Perdew, K. Burke, and M. Ernzerhof, *Phys. Rev. Lett.* **77**, 3865 (1996).
- [139] G. Pizzi *et al.*, *J. Phys.: Condens. Matter* **32**, 165902 (2020).
- [140] N. Marzari, A. A. Mostofi, J. R. Yates, I. Souza, and D. Vanderbilt, *Rev. Mod. Phys.* **84**, 1419 (2012).
- [141] A. A. Mostofi, J. R. Yates, Y.-S. Lee, I. Souza, D. Vanderbilt, and N. Marzari, *Comput. Phys. Commun.* **178**, 685 (2008).
- [142] J. Kuneš, R. Arita, P. Wissgott, A. Toschi, H. Ikeda, and K. Held, *Comput. Phys. Commun.* **181**, 1888 (2010).
- [143] See [https://github.com/AbinitioDGA/ADGA/blob/master/srvo3-testdata/srvo3\\_k20.hk](https://github.com/AbinitioDGA/ADGA/blob/master/srvo3-testdata/srvo3_k20.hk).
- [144] P. Pulay, *Chem. Phys. Lett.* **73**, 393 (1980).
- [145] P. Császár and P. Pulay, *J. Mol. Struct.* **114**, 31 (1984).
- [146] We thank Patrik Thunström for drawing our attention to this crucial insight.
- [147] K. Astleithner, A. Kauch, T. Ribic, and K. Held, *Phys. Rev. B* **101**, 165101 (2020).
- [148] G. V. Astretsov, G. Rohringer, and A. N. Rubtsov, *Phys. Rev. B* **101**, 075109 (2020).
- [149] F. Krien, A. Valli, P. Chalupa, M. Capone, A. I. Lichtenstein, and A. Toschi, *Phys. Rev. B* **102**, 195131 (2020).